



UNIVERSITY OF LEEDS

This is a repository copy of *Structural Insight into Eukaryotic Sterol Transport through Niemann-Pick Type C Proteins*.

White Rose Research Online URL for this paper:
<http://eprints.whiterose.ac.uk/150541/>

Version: Accepted Version

Article:

Winkler, MBL, Kidmose, RT, Szomek, M et al. (5 more authors) (2019) Structural Insight into Eukaryotic Sterol Transport through Niemann-Pick Type C Proteins. *Cell*, 179 (2). 485-497.e18. ISSN 0092-8674

<https://doi.org/10.1016/j.cell.2019.08.038>

© 2019, Elsevier. This manuscript version is made available under the CC-BY-NC-ND 4.0 license <http://creativecommons.org/licenses/by-nc-nd/4.0/>.

Reuse

This article is distributed under the terms of the Creative Commons Attribution-NonCommercial-NoDerivs (CC BY-NC-ND) licence. This licence only allows you to download this work and share it with others as long as you credit the authors, but you can't change the article in any way or use it commercially. More information and the full terms of the licence here: <https://creativecommons.org/licenses/>

Takedown

If you consider content in White Rose Research Online to be in breach of UK law, please notify us by emailing eprints@whiterose.ac.uk including the URL of the record and the reason for the withdrawal request.



eprints@whiterose.ac.uk
<https://eprints.whiterose.ac.uk/>



AARHUS UNIVERSITY



Coversheet

This is the accepted manuscript (post-print version) of the article.

Content wise, the accepted manuscript version is identical to the final published version, but there may be differences in typography and layout.

How to cite this publication

Please cite the final published version:

Winkler MBK, Kidmose RT, Szomek M, Thaysen K, Rawson S, Muench SP, Wüstner D, Pedersen BP. (2019) Structural insight into eukaryotic sterol transport through Niemann-Pick type C proteins. Cell 179(2): 485-497.e18.

Publication metadata

Title:	<i>Structural insight into eukaryotic sterol transport through Niemann-Pick type C proteins</i>
Author(s):	<i>Mikael B. L. Winkler, Rune T. Kidmose, Maria Szomek, Katja Thaysen, Shaun Rawson, Stephen P. Muench, Daniel Wüstner, Bjørn Panyella Pedersen</i>
Journal:	<i>Cell</i>
DOI/Link:	https://doi.org/10.1016/j.cell.2019.08.038
Document version:	Accepted manuscript (post-print)
Document license:	CC-BY-NC-ND license https://creativecommons.org/licenses/by-nc-nd/4.0/

General Rights

Copyright and moral rights for the publications made accessible in the public portal are retained by the authors and/or other copyright owners and it is a condition of accessing publications that users recognize and abide by the legal requirements associated with these rights.

- Users may download and print one copy of any publication from the public portal for the purpose of private study or research.
- You may not further distribute the material or use it for any profit-making activity or commercial gain
- You may freely distribute the URL identifying the publication in the public portal

If you believe that this document breaches copyright please contact us providing details, and we will remove access to the work immediately and investigate your claim.

If the document is published under a Creative Commons license, this applies instead of the general rights.

Title

Structural insight into eukaryotic sterol transport through Niemann-Pick type C proteins

Authors

5 Mikael B. L. Winkler¹, Rune T. Kidmose¹, Maria Szomek², Katja Thaysen², Shaun Rawson^{3,4}, Stephen P. Muench³, Daniel Wüstner², Bjørn Panyella Pedersen^{1,5,6*}

Affiliations

- 10 1) Department of Molecular Biology and Genetics, Aarhus University, Gustav Wieds Vej 10, Aarhus C, DK-8000, Denmark.
- 2) Department of Biochemistry and Molecular Biology, University of Southern Denmark, Campusvej 55, Odense M, DK-5230, Denmark.
- 3) School of Biomedical Sciences & Astbury Centre for Structural and Molecular Biology, University of Leeds, Leeds, LS2 9JT, United Kingdom.
- 15 4) Current Address: Department of Biological Chemistry and Molecular Pharmacology, Harvard Medical School, Boston, Massachusetts 02115, USA.
- 5) Aarhus Institute of Advanced Studies, Aarhus University, Høegh-Guldbergs Gade 6B, Aarhus C, DK-8000, Denmark.
- 6) Lead Contact.
- 20 * Correspondence: bpp@mbg.au.dk

Summary

Niemann-Pick type C (NPC) proteins are essential for sterol homeostasis, believed to drive sterol integration into the vacuolar/lysosomal membrane before redistribution to other cellular membranes. Here, using a combination
25 of crystallography, cryo-electron microscopy, biochemical and *in vivo* studies on the *Saccharomyces cerevisiae* NPC system, NCR1/NPC2, we present a framework for sterol membrane integration. Sterols are transferred between hydrophobic pockets of vacuolar NPC2 and membrane-protein NCR1. NCR1 has its N terminal domain (NTD) positioned to deliver a sterol to a tunnel connecting NTD to the luminal membrane leaflet 50 Å away. A sterol is caught inside this tunnel during transport, and a proton-relay network of charged residues in the
30 transmembrane region is linked to this tunnel supporting a proton-driven transport mechanism. We propose a model for sterol integration which clarifies the role of NPC proteins in this essential eukaryotic pathway and which rationalizes mutations in patients with Niemann-Pick disease Type C.

INTRODUCTION

35 Sterols are an essential component of membranes in all eukaryotic cells. In humans, Niemann-Pick type C proteins NPC1 and NPC2 bind cholesterol and are essential for lysosomal membrane integration from where cholesterol is redistributed to other cellular membranes (Carstea et al., 1997; Loftus et al., 2002; Naureckiene et al., 2000). Disturbance of this pathway leads to Niemann-Pick disease Type C, a neurodegenerative disease where cholesterol and other lipids accumulate in the lysosomes (Pentchev, 2004). Furthermore, NPC1 has been
40 identified as a key virulence factor for the Filoviruses Ebola and Marburg (Carette et al., 2011; Côté et al., 2011). The molecular mechanism of sterol membrane integration is still unclear, despite having been studied extensively. NPC2, a soluble intra-lysosomal protein, binds sterols with distinct polarity (polar head-group exposed and aliphatic tail buried in the cavity), and is able to hand-off this sterol to the luminal N terminal domain (NTD) of the lysosomal membrane protein NPC1 with reversed polarity (polar head-group buried in the
45 pocket) (Deffieu and Pfeffer, 2011; Friedland et al., 2003; Kwon et al., 2009; Wang et al., 2010; Xu et al., 2007). Through an unknown mechanism the sterol bound to the NTD is then believed to be passed to the lysosomal membrane for integration (Davies and Ioannou, 2000; Davies et al., 2000). Several sterol binding sites have been suggested in NPC1, and sterol integration into the membrane involves a membrane-buried Sterol Sensing Domain (SSD), but the structural and functional relationship between these sites in NPC proteins remains
50 unknown (Lu et al., 2015; Ohgami et al., 2004; Ohgane et al., 2013). The luminal side of the lysosomal membrane is covered in a ~60 Å thick glycocalyx, a polysaccharide matrix coating which preserves the integrity of the lysosomal membrane protecting the cytosol from degradative enzymes inside the lysosome lumen. It has been speculated that NPC1 could help sterols bypass this protective layer (Gong et al., 2016; Li et al., 2016a; Neiss, 1984; Pfeffer, 2019). In yeast this degradation process is delegated to the vacuole (Schulze et al., 2009).
55 The *S. cerevisiae* NCR1/NPC2 system, located in the yeast vacuole, has been studied extensively to obtain insight into the function and dynamics of NPC proteins, and both NPC1 and NPC2 deficient mammalian cells can be rescued by the *S. cerevisiae* counterpart (Berger et al., 2005a, 2005b; Jacquier and Schneiter, 2012; Malathi et al., 2004; Munkacsı et al., 2011; Tsuji et al., 2017). The NCR1/NPC2 system shares 32%/22% sequence identity with the human system (hNPC1/hNPC2), but there is no structural framework to relate NCR1
60 and NPC2 to their human counterparts at the molecular level (Figures S1 and S2A). Clues to the mechanism of sterol uptake can be found in the cryo-EM structure of the full length hNPC1 (Gong et al., 2016), the crystal structure of a large fragment of hNPC1 without the NTD (Li et al., 2016a), and the crystal structure of the middle luminal domain (MLD) domain of hNPC1 bound to hNPC2 (Li et al., 2016b). Furthermore, recent breakthroughs in the related Patched protein family belonging to the same Resistance-
65 Nodulation-Division (RND) superfamily as NPC1 proteins, also provide hints towards a possible common core-mechanism, since Patched is involved in a reverse process of sterol extraction from the membrane (Gong et al., 2018; Qi et al., 2018a, 2018b; Zhang et al., 2018). Despite this, we do not have a clear understanding of how

NPC1 and NPC2 mediate transfer of sterols into the lysosomal membrane, and several different models currently co-exist (Li et al., 2016a; Pfeffer, 2019; Trinh et al., 2018).

70 Here we present four structures of yeast NCR1 and NPC2. The crystal structure of NPC2 is solved in both a sterol-free and sterol-bound state. We measure sterol binding affinities and demonstrate that sterol transfer is possible between NPC2 and the NTD of NCR1. We show that one physiological function of NPC2 and NCR1 is to deliver sterols to the vacuole in living yeast cells, in analogy to the human system. The structures of NPC2 rationalize how sterols are captured and shuttled in the yeast vacuole, and they display an expanded binding site
75 compared to its human counterpart indicative of a broader substrate range. We also present the first crystal structure, as well as the first single particle cryo-EM structure, of NCR1. Both structures adopt a novel conformation not observed in the human NPC1. We identify a tunnel through the central core of NCR1 that links the NTD with the SSD and in which we observe a bound sterol. Based on our data we propose a mechanism for sterol transport where NCR1 can bypass the glycocalyx via a tunnel to mediate sterol insertion into the
80 membrane. The model explains puzzling results in the field related to the number of sterol binding sites, and it offers a rationale for why the sterol polarity switch from NPC2 to NTD is necessary for proper membrane integration in vivo. Finally, our data suggest that the molecular mechanism of sterol transfer and sterol membrane integration is conserved from fungi to humans, and offers a rationale for missense mutations found in patients with Niemann-Pick Disease Type C.

85

RESULTS

Structure of sterol-free and sterol-bound NPC2

We expressed, purified and crystallized *S. cerevisiae* NPC2 (Figure S2B; see also Table S1). The sterol-free form of NPC2 is determined by experimental phasing to 2.8 Å (R_{free} 26.2%) with 3 identical monomers (RMSD_(CA) < 0.33 Å) in the asymmetric unit forming a trimer with 120 degree rotational symmetry. In the crystal packing, a propeptide (residue 24-34) from one monomer of the trimer extends to fold over a neighboring monomer from another trimer (Figure S2C). The NPC2 monomer adopts an open Ig-like beta-sandwich fold with seven anti-parallel beta-strands (Figure 1A). Strand 1, 2 and 5 form one side of the sandwich while strand 3, 4, 6 and 7 form the other. A small alpha helix between strand 4 and 5 forms a cover (residues 109-123) enclosing part of a deep and elongated hydrophobic cavity (1019 Å³) between the two sides of the sandwich, leaving space for substrate
95 entry and exit at only one end of the sandwich. Two disulfide bonds and a single N-linked glycosylation stabilize the structure.

The structure of NPC2 in complex with sterols was determined to 2.9 Å (R_{free} 25.7%) (Figures 1B and S2D; see also Table S1). The asymmetric unit contains 9 monomers forming 3 trimers similar to the trimer in the sterol-free structure, but without the propeptide interaction between trimers (Figure S2E). A single ergosterol molecule
100 is found in the hydrophobic binding cavity in 5 of the monomers, while the remaining 4 monomers have strong

density features in the binding cavity that cannot be confidently classified but appear to be bulkier than ergosterol, and may be other lipids (Figure S2F and S2G). The sterol polarity within the cavity is such that the polar headgroup points out and the aliphatic tail into the cavity in the same orientation as observed in previous human and bovine NPC2 structures (Figure S2H) (Li et al., 2016b; Xu et al., 2007). The sterol resides in a hydrophobic cavity lined by the side chains of Pro67, Leu73, Val95, Leu102, Leu103, Ile138, Val142, Tyr147, Val149, Val168 and Phe170 some of which form non-specific hydrophobic interactions between NPC2 and the sterol (Figure 1C). The cavity is of sufficient size that two sterols could fit side-by-side in the opening, but such a setup is not supported by the observed density (Figures S2G and S2I). There is no difference in conformation of sterol-free and sterol-bound NPC2 ($\text{RMSD}_{(\text{CA})} < 0.3 \text{ \AA}$) (Figure 1B), similar to the bovine sterol-free vs sterol-bound NPC2 (Xu et al., 2007). While yeast NPC2 has a similar sandwich fold and almost identical binding of a single sterol as human and bovine NPC2, the global structure displays significant differences (e.g. to bovine sterol-bound form $\text{RMSD}_{(\text{CA})} 3.0 \text{ \AA}$) (Figure S2H). NPC2 has a much larger binding cavity compared to human and bovine NPC2 because it lacks a disulfide bond that in the human and bovine NPC2 pushes the beta-sandwich together opposite the sterol binding site. Furthermore, multiple bulky side chains are facing the cavity in both human and bovine NPC2 but not in yeast NPC2, reducing the size of these cavities (e.g. bovine NPC2 cavity: 186 \AA^3) (Figures 1D). Despite this, the observed sterol binding site in all three is very similar with respect to position and orientation of the sterol, with a small difference being a slight tilt of the sterol in yeast NPC2 compared to bovine and human NPC2 (Figure 1E). It has previously been shown that yeast NPC2 can rescue human NPC2-deficient fibroblasts (Berger et al., 2005b), and we can now rationalize this, as essential components of sterol binding are conserved between yeast NPC2 and human NPC2.

Sterol binding and transfer by the NCR1/NPC2 system

To establish the binding properties of the NCR1/NPC2 system, we assayed binding affinities of NPC2 and the NTD of NCR1 using two different approaches; i) Förster resonance energy transfer (FRET) from aromatic residues to an intrinsically fluorescent ergosterol analog, dehydroergosterol (DHE), and ii) binding of radiolabeled cholesterol. When exciting NPC2 at 280 nm, sterol binding can be detected as fluorescence of DHE emitting between 360–400 nm with three characteristic peaks (Figure S3A). This FRET effect from NPC2's Tyr and Phe shows that DHE binds to NPC2 with nanomolar affinity ($K_d = 121 \text{ nM}$) (Figure 2A). Using radiolabeled cholesterol in a different experimental setup, we observe a binding affinity in the same nanomolar range ($K_d = 591 \text{ nM}$) (Figures 2B). Binding competition assays show that the antifungal lipid edelfosine interferes strongly with cholesterol binding, while the hNPC1 inhibitor U18666A and the cholesterol trafficking inhibitor Cepharanthine inhibit binding more weakly (Figure 2C). In combination with the large binding cavity observed in the crystal structure, this data suggests that yeast NPC2 could be involved in general hydrophobic substrate trafficking, but this needs to be investigated further in order to identify which substrates it shuttles.

We expressed and purified NTD and measured DHE binding (FRET) and cholesterol binding (radiolabel) and observed similar binding affinities, $K_d = 483$ nM and 675 nM respectively, with both assays (Figures 2D, 2E and S3B). Binding competition assays show that the antifungal lipid edelfosine competes strongly with binding of radiolabeled cholesterol, while U18666A and Cepharanthine have weaker effects (Figure 2F).

140 We examined sterol transfer between NPC2 and NTD using FRET. Because NPC2 contains no tryptophans, we can specifically measure binding of DHE to NTD when exciting NTD's Trp at 295 nm (Figures S3C and S3D). NPC2 is able to transfer DHE to NTD, while NTD as sterol donor can transfer to NPC2 as well (Figure 2G, S3E and S3F). NPC2 is able to transfer radio-labeled cholesterol both to the NTD and to other NPC2 molecules (Figure 2H). NTD as a cholesterol donor can transfer to NPC2, and also to other NTD molecules, if somewhat
145 less efficiently (Figure 2I). Finally, we reproduced the transfer of cholesterol from NPC2 to NCR1 using full-length NCR1. We are able to clearly observe a transfer from NPC2 to NCR1 that is dependent on the presence of the NTD (Figure 2J). These observations for yeast NCR1/NPC2 are comparable to the behavior of the hNPC1/hNPC2 proteins underlining the similarities between the two systems (Infante et al., 2008).

150 **Structure of NCR1**

The crystal structure of full length NCR1 was solved to 3.5 Å with the asymmetric unit containing a single molecule with no indication of oligomerization. The final model is refined to an R_{free} of 30.1% and includes residues 21-1159 (of 1170 total). The electron density allows unambiguous building of NCR1, except for two
155 disordered loops (residues 280-315 and 729-735) (Figure S4A; see also Table S1). The density clearly reveals a single bound ergosterol, as well as four N-linked glycosylations and fourteen disulfide bridges in the structure (Figure S4B). NCR1 consist of four domains (Figure 3A): the NTD, the transmembrane domain (M2-M13), the middle luminal domain (MLD), and the C terminal domain (CTD).

The transmembrane region is comprised of 13 transmembrane helices with M1 in an isolated position. M2-M13
160 comprise the transmembrane domain, and here, M2-M7 and M8-M13 share a pseudo two-fold rotational symmetry around an axis perpendicular to the membrane (Figure 3B). M3-M7 comprises the canonical sterol sensing domain, but structurally it is clear that M2 should also form part of the sterol sensing domain (SSD, residues 338-358+530-719) (Figure S4C). This first helix of the SSD was missed in the original sequence analysis of SSD-containing proteins due to its lack of proximity to the rest of the SSD in amino acid sequences (Hua et al., 1996; Kuwabara and Labouesse, 2002). The SSD has a shelf-like pocket exposed to the outer leaflet
165 of the membrane spanned by M2-M5 of sufficient size to harbor a single sterol molecule (Figures 3B, 3C and S4C). Two acidic residues are buried in the transmembrane domain, Asp631(M5) and Glu1068(M11) and are fully conserved in all NPC family members. In the structure they point towards each other at the center of the pseudo-symmetric related transmembrane helices with a distance of 3.9 Å between them, suggesting that either or both of these acidic residues are protonated. In close proximity to Asp631 and Glu1068 we find

170 His1072(M11) 3.3 and 2.6 Å away respectively (Figure 3D). Asp631 and Glu1068 are the only conserved and buried charged residues in the transmembrane domain, and together with His1072 they form a proton-relay network which suggests a functional role of this cluster in NCR1. This is supported by mutagenesis with H1072A and D631N mutants both showing a reduction in transfer of cholesterol despite being at a distance of around 80 Å from the NTD (Figure 2J). The impact of distant residues in NCR1 on sterol loading from NPC2
175 might suggest an allosteric coupling from this transmembrane proton site via the CTD and MLD to the NTD. The MLD and CTD form a joint structure that point into the lumen of the vacuole with a size that allow it to penetrate the glycocalyx. The MLD and the CTD are related by a pseudo two-fold symmetry, with 7 conserved secondary structure elements forming a sandwich against each other. Inserted into the sequence of this conserved sandwich of both MLD and CTD are a region of 80 and 101 amino acids respectively, that form two hyper-
180 variable regions which are presented to the vacuolar space creating a docking surface to binding partners (Figures 3A, S1 and S4D). The MLD and the CTD are attached to the transmembrane domain via four neck helices from M2 and M3 to MLD and M8 and M9 to CTD (Figure 3C). The M2 and M8 connections form two elongated structures perpendicular to the membrane plane and interact closely with the M5/M11 loops. The two 'coupling-loops' directly link the MLD and CTD to the central pseudo-twofold acidic pair buried in the
185 membrane. Together, the MLD/CTD domains form a luminal core that the NTD docks to at the top of the pseudo two-fold symmetry point.

The NTD is coupled to the rest of NCR1 via a long linker (~45 Å) that contains three internal disulfide bridges and connects via transmembrane helix M1 and a long cytosolic loop to Cytosolic Helix 1 before the SSD (Figure 3A). M1 has a noticeable tilt away from the transmembrane domain towards the cytosolic side. Contact to the
190 transmembrane domain is achieved by pi-stacking between Tyr266(M1) and Phe761(M8), and a hydrogen bond between Ser259(M1) and the main chain oxygen of Val765(M8) (Figure 3B). The tilt of M1 in hNPC1 is reduced by about 20 degrees compared to NCR1 (Figure S4E).

The sterol binding core of the NTD is similar to the human NTD with a backbone RMSD_(CA) of 2.2 Å. The NTD has a clearly defined sterol binding pocket and, as in the cryo-EM hNPC1 structure, the binding pocket is empty
195 (Figure S4F). The pocket has a size of 201 Å³, much smaller than the cavity in NPC2, providing an explanation for the observed differences in transfer efficiency and competition assays. Compared to the cryo-EM hNPC1 structure the position of the NTD is significantly different with a rotation of the binding pocket towards the MLD/CTD two-fold point of about 20 degrees and a tilt of 40 degrees, which positions the pocket directly towards the MLD/CTD two-fold point (Figure 4A). This rotation relative to the MLD/CTD leads to a loop-helix
200 motif (residue 157-172) of the NTD moving by ~14 Å towards the MLD/CTD two-fold point, where it now forms an interaction surface to the side of the CTD. This weak interaction is mediated mainly by a hydrogen bond from Ser162(NTD) to Asn865(CTD) as well as hydrophobic interactions. To test the impact of this interaction on NTD's ability to accept sterols from NPC2, we mutated Asn865 of this interaction surface

(N865A, removing the hydrogen bond). This mutant display reduced transfer from NPC2 to NCR1 (Figure 4B), supporting the notion that this region is involved in the conformational shift of the NTD to accept sterols from NPC2. The loop-helix motif starts after a conserved disulfide bridge (Cys101-Cys156) at the end of an alpha helix, and ends before a conserved and flexible glycine hinge of 1-3 glycines (residues 173-175) found in all NTD domains that appear to help control the movement of the loop-helix motif and the NTD relative to the rest of NCR1. We analyzed the glycine hinge both by deletion and by mutagenesis to a tri-alanine stretch and in both cases we observed a strong reduction in the ability of NPC2 to transfer sterols to NCR1 (Figure 4B). This is consistent with the structural data that suggest a pivotal role of the glycine hinge in the conformational shifts of NTD allowing for sterol loading and unloading. The combination of the described M1 tilt and the rotated position of the NTD towards the MLD/CTD in our NCR1 structure result in a new conformation with implications for the function of these domains in sterol loading.

Recently, structures from the Patched protein family have revealed the presence of a tunnel in the MLD/CTD region of Patched through which cholesterol might be transferred (Gong et al., 2018; Qi et al., 2018a; Zhang et al., 2018). We find a similar tunnel in NCR1 at the pseudo two-fold symmetry point of the MLD and CTD (Figure 4C). The residues comprising the tunnel are the most conserved of NCR1, supporting an indispensable role (Figure S5A). The tunnel extends from the membrane leaflet and the SSD shelf to the 157-172 loop-helix motif of NTD which are positioned below the tunnel mouth and appear to block it as a gate (Figure 4D). In NTD, the sterol binding site is a direct continuation of this tunnel. Inside the tunnel between MLD and CTD we observe density for an ergosterol 24 Å from the start of the membrane (Figure 4E). The sterol is positioned with the hydroxyl group pointing towards the NTD and the aliphatic chain towards the SSD, which match the polarity of a NTD deposited sterol released into the tunnel. The polar part of ergosterol does not coordinate to any residues, but a small rotation of the nearby Arg950(CTD) could provide an interaction with the hydroxyl group. The NTD loop-helix gate appears to prevent sterol back-flow, but it is possible that a sterol could be moved around it. The chemical environment of the tunnel does not appear to support fixed binding sites for sterols, but rather forms a continuous hydrophobic environment, with a few areas of hydrophilic nature. In support of this, the occupancy of the observed sterol refines to 0.87 in the crystal structure, corresponding to a flexible binding (Figure S5B). Based on this structural analysis, the crystal conformation of NCR1 represents a “sterol post-loading state”, where the sterol bound in the NTD has been deposited into the tunnel for transfer to the SSD and integration into the membrane. This conformational state is different from the previously reported conformation found in the cryo-EM hNPC1 structure, that appears to represent an “empty pre-loading state” ready to accept sterols from NPC2 (Gong et al., 2016).

We determined the structure of NCR1 by single particle cryo-EM in parallel with the crystal structure. The reconstruction has a global resolution of 7.2 Å including the detergent micelle, with most protein regions extending to 5-6 Å (Figure 5). Docking the crystal structure into the EM map, shows strong similarity to the

crystallographic model of NCR1 (RMSD_(CA) 1.5 Å) (Figure 5C). Interestingly, the NTD is slightly shifted which likely relates to the flexible nature of this domain, but it still retains the sterol pocket opening in the same
240 position, and the NTD loop-helix gate is unchanged (Figures S5C and S5D). A tunnel between MLD and CTD is also found in the fitted cryo-EM NCR1 model, but there is no indication of a sterol density in the map, as is expected due to the low resolution. Overall, the NTD is in a similar position as in the crystal structure, and clearly differs from the cryo-EM hNPC1 conformation (Figure S5E). The cryo-EM structure is free from any crystal contacts, supporting that the position of the NTD in the crystal structure is not influenced by crystal
245 packing.

NCR1/NPC2 delivers sterols to the vacuolar membrane in analogy with the mammalian system

To determine the physiological function of the yeast NCR1/NPC2 system and its relationship to NPC1/NPC2 in mammalian cells we developed an *in vivo* assay to monitor sterol transport directly from the plasma membrane
250 to the vacuole. Sterol transport can be studied using live-cell imaging of the fluorescent ergosterol analog DHE, and we hypothesized that aberration of DHE transport could be examined in starved NCR1/NPC2-deficient yeast cells, when cells become dependent on lipophagy, a special form of autophagy.

Our results show that yeast transport sterols from the plasma membrane to specialized cellular lipid storage organelles, called lipid droplets, which become ingested by vacuoles during starvation (Figures 6A and S6).
255 NCR1 and NPC2 are required for transfer of sterol from lipid droplets to the vacuolar membrane, as absence of either of these proteins result in disposition of DHE in large non-digested lipid droplets inside and outside of vacuoles without labeling of the vacuolar membrane (Figure 6). In starved wild type cells, DHE is primarily found in the vacuolar membrane with some diffuse staining in the vacuole lumen indicating complete digestion of the lipid droplets (Figures 6 and S6). In contrast, in starved cells lacking NCR1 or NPC2, the vacuole is
260 fragmented with an irregular shape, and numerous large lipid droplets are found outside and inside the vacuole (Figures 6 and S6). The results demonstrate that NCR1- and NPC2-deficient cells internalize lipid droplets into their vacuoles, but further processing of lipid droplets and transport of sterols to the vacuolar membrane is impaired *in vivo*.

To probe the effect of pH and proton gradient on this process we next inhibited the vacuolar proton pump using
265 Concanamycin A. This result in a vacuolar sterol phenotype identical to the phenotype observed for NCR1- and NPC2-deficient cells (Figure 6). These results show that sterol delivery to the vacuolar membrane by the NCR1/NPC2 system is instrumental for normal function of the vacuole, and disturbance of the pH environment creates an identical phenotype. Analogous observations have been made for mammalian NPC1 underlining the similarities between the two systems (Sarkar et al., 2013).

270

DISCUSSION

Ligand specificity of NPC2 and NTD and the loading complex of the NCR1/NPC2 system

We report the first structures of both the soluble and membrane integrated components of the yeast sterol-transporting NCR1/NPC2 system. We show that NPC2 is able to bind sterols in a similar fashion as human and bovine NPC2 and with comparable affinity, and that it is able to transfer sterols to the NTD of NCR1. This resembles observations made for hNPC2 and for the NTD of hNPC1 (Infante et al., 2008; Kwon et al., 2009). The ligand competition assays and the large size of the NPC2 cavity further suggest an additional role for NPC2 as a more general hydrophobic binding partner in the vacuolar environment. The yeast NCR1/NPC2 system might transport other lipids besides sterols, and additionally have a more general and promiscuous lipid/sterol capture-and-shuttle function inside the vacuole, supported by evidence that NPC proteins interact with other cytoplasmic sterol shuttling proteins (Du et al., 2011). NCR1^{-/-} yeast strains are resistant to the lipid-drug Edelfosine (Berger et al., 2005a), implying it cannot integrate into the vacuolar membrane unless channeled by NCR1, and this is now supported by our observation that both NPC2 and NTD bind Edelfosine.

The position and flexibility of the NTD appear to be a central feature of the function of NPC proteins. A NCR1/NPC2 loading conformation requires that the NTD is rotated significantly towards the MLD to receive sterols from NPC2. This can be modeled if we rotate NCR1's NTD to match the position found in the hNPC1 cryo-EM structure in the empty pre-loading state. hNPC2 as well as Ebola virus glycoprotein interact with two loops protruding from the variable region of the MLD of hNPC1 (Li et al., 2016b; Wang et al., 2016). However, this interaction point is not sufficient to create a tight transfer complex from hNPC2 to the NTD based on the structures solved so far, and the residues in the observed MLD/hNPC2 complex do not match residues found to be implicated in actual transfer (Gong et al., 2016; Wang et al., 2010). These interacting loops from the variable region of the MLD are not conserved from human NPC1 to yeast NCR1 (Figure S5F). It is possible that the MLD interaction points identified in the hNPC2/MLD complex represent an early stage of complex formation, and also that the yeast system NCR1/NPC2 loading complex is initiated differently.

A tunnel to bypass the glycocalyx and possible active movement of sterols within it

The position of the NTD towards a sterol-loaded MLD/CTD tunnel in NCR1 highlights novel aspects about NPC mediated sterol integration into lysosomal/vacuolar membranes. The tunnel explains how sterols bypass the glycocalyx to reach the membrane for integration by linking the NTD and SSD to each other, and it explains several puzzling observations in the NPC family, where data has been inconclusive regarding the number of sites (e.g. Lu et al., 2015; Ohgami et al., 2004; Ohgane et al., 2013), Patched proteins might employ a related transport mechanism, and sterol-like densities have been observed inside analogous tunnels of Patched (Zhang et al., 2018). There are at least two possible molecular mechanisms that could drive sterol displacement through the tunnel; either passive diffusion, or active transport mediated by pincer-like movements of the MLD and CTD

domains. We show that residues at the proton-relay site influence sterol transfer from NPC2 to full length NCR1, suggesting that proton translocation could accompany sterol transport by the NCR1/NPC2 system. An active mechanism would almost certainly be driven by the coupling loops that connect the MLD and CTD to the Asp632/Glu1068/His1072 cluster in the transmembrane region (Figures 3B and 3D). The same mechanism for active transport has been proposed for several other proteins that belong to the RND super-family such as MmpL3 and HpnN (Kumar et al., 2017; Su et al., 2019; Zhang et al., 2019), and is well characterized in particular in the proton driven exporter AcrB (Zhang et al., 2017). In AcrB, conformational changes linking the transmembrane region and the extracellular domains have been demonstrated as the primary mechanistic parameter for proton-driven transport. AcrB is an obligate trimer and has a transport pathway through a cavity in its 'Porter' domain, homologous to the MLD/CTD of NCR1. Importantly, the tunnel we observe in NCR1 is in the same location as the AcrB transport pathway (Figure S7) and both published structures of hNPC1 contain similar tunnels according to our analysis (Figures S7D and S7E). For NCR1, hNPC1 and Patched the tunnels are unrestricted, while in AcrB, the tunnel-cavity switches between three conformational steps, depending on the protonation state of a transmembrane proton donor/acceptor pair (Asp407/Lys940) located at the transmembrane two-fold point. Proton translocation at this proton-relay point result in movement of the transmembrane helices and a displacement of the perpendicular coupling helices with consequent changes to the Porter domain (Zhang et al., 2017). In NCR1, the corresponding proton-relay residues are the Asp632/Glu1068/His1072 cluster, and these 3 central residues of the transmembrane domain are fully conserved in the rest of the NPC family as well as the Patched family (Figures 3D, S1 and S7). The NPC and Patched families could use the conserved histidine to control pKa of the acidic residues buried here (Buch-Pedersen et al., 2009). In support of this, a comparative analysis of Patched with hNPC1 has revealed a displacement of neck helices in both proteins which match elements of the proton/substrate transport coupling mechanism found in AcrB (Gong et al., 2018). There is no direct evidence for proton translocation as a necessity to drive sterol integration in either the NPC or Patched families, but there are some strong indications: 1) In NPC1, a link has been suggested between transmembrane movement of charge and transport by demonstrating proton driven transport of oleic acid (Davies et al., 2000). 2) Inhibiting the V-type ATPase and thereby removing the proton motive force from lysosomal membranes leads to cholesterol buildup in the lysosomal lumen (Furuchi et al., 1993; Ouimet et al., 2011; Sarkar et al., 2013). 3) Patched transport is highly sensitive to CCCP, a proton motive force decoupler, and the transmembrane mutant G509V/D513Y, targeting the transmembrane acidic cluster, has significantly lowered transport of the chemotherapeutic agent doxorubicin (Bidet et al., 2012). 4) Our *in vivo* results demonstrate a strong dependence on the pH environment for correct sterol transport to the vacuole membrane (Figure 6) 5) Our biochemical results on the proton-relay residues of the transmembrane helix also demonstrate a negative effect on sterol transfer by NCR1 (Figure 2J). There is thus indirect but strong evidence of a proton-driven transport mechanism

340 in the literature, which is supported by key elements of our NCR1 structure and by our biochemical and *in vivo* data.

Model of sterol integration into the membrane

345 Based on the presented results we propose the following model for sterol transport (Figure 7): 1) Sterols in the lysosomal/vacuolar lumen are captured by NPC2 with the aliphatic tail buried in the binding cavity. 2) NPC2 transfers the sterol to the NTD of NCR1 where the sterol binds in the polar opposite direction. 3) The NTD rotates to align the NTD binding pocket to the MLD/CTD tunnel which could be linked to the M1 tilt angle. 4) The sterol is transported through the tunnel to the SSD shelf likely by pincer movements driven by proton interactions with the transmembrane Asp/Glu pseudo-symmetry pair, as controlled by the conserved histidine. 5) From the SSD, the sterol diffuses into the outer leaflet of the lipid bilayer, ready for transport to other cellular membranes.

350 There has been an ongoing debate on the mechanism of sterol integration into the lysosomal/vacuolar membrane. The presented tunnel-based model is distinct to previously proposed models in which the NTD decouples from the MLD/CTD upon binding of a sterol and folds in towards the membrane to embed the sterol directly, or via the SSD, into the membrane (Li et al., 2016a; Trinh et al., 2018).

355 Our model is strengthened by the observation that many fungi have the NTD as a separate soluble protein, while still retaining NPC2, implying that NPC2 cannot directly deposit its cargo to NCR1 without the NTD being present (Adebali et al., 2016). In our model, the transfer from NPC2 to the NTD is needed to reorient the sterol allowing it to pass through NCR1 with the aliphatic chain first for integration into the membrane. There are studies that show that hNPC2 is able to deposit sterols directly into bilayers, bypassing hNPC1 in artificial systems without a glycocalyx (Enkavi et al., 2017; Infante et al., 2008; Xu et al., 2008). We suggest that a first basic step in sterol homeostasis is the capture and trafficking of sterol monomers by NPC2 after hydrolysis of sterol esters inside the vacuole/lysosome. One major role of NCR1/hNPC1 is to facilitate monomeric sterols donated by NPC2 to bypass the glycocalyx for integration into the vacuole/lysosome membrane.

365 NCR1/NPC2 as a model system for mammalian NPC1/NPC2 and mutations in NPC patients

We found that the NCR1/NPC2 system is required to deliver sterols from lipid droplets to the vacuole under starvation conditions of yeast cells. This observation of a NCR1/NPC2 specific yeast sterol storage phenotype during lipophagy aligns with recent observations from mammalian cells; macrophages contain sterol rich lipid droplets, and the mobilization of this sterol pool requires lysosomal digestion of these droplets during autophagy. Collapsing the pH gradient across the lysosomal membrane inhibits this process leading to cholesterol build up in endo-lysosomes (Furuchi et al., 1993; Ouimet et al., 2011). Mammalian cells lacking NPC1 display impaired autophagy with observations of both reduced autophagosome-lysosome fusion and accumulation of lipid

droplets. Inhibition of lysosome acidification using bafilomycin A in cells expressing functional NPC1 leads to the same phenotype (Sarkar et al., 2013). This is in accordance with our results on the yeast system using a
375 NCR1 deficient strain or Concanamycin A. Our results show that the concerted function of the NPC system in sterol transport and autophagy is conserved between yeast and mammalian cells, suggesting that an ancient evolutionary function of the system might be sterol mobilization during autophagy. In both systems, sterol transport strictly depends on an actively maintained proton gradient across the lysosomal/vacuolar membrane, strengthening our model of proton-dependent sterol transport by NPC proteins.

380 Based on our model for transport we can now provide a mechanistic rationale behind defects in single-point mutations found in patients with NPC disease. By our survey, there are at least 154 identified missense mutations in the NPC1 protein that lead to Niemann-Pick disease type C (Table S2). Our structural analysis of the NPC disease mutations suggests a direct link to pivotal mechanistic elements of NPC1 sterol transport that we can classify into four categories (Figure S7H and Figure S7I): 1) Direct effect on the suggested proton-relay site, 2)
385 Interference with the sterol pathway, 3) Interference with the structural elements that link the sterol tunnel to the transmembrane proton-relay site driving the suggested pincher movement, and 4) Surface located mutations with no clear mechanistic implication related to the proposed transport model. This final group is heavily biased toward the MLD and CTD domains and could be involved in interaction sites to other proteins, to folding or stability. Of the 139 plotted residues, whose mutation leads to NPC disease, 64 are identical between the human
390 and yeast NPC systems, and another 23 have conserved biochemical properties (63% total). The most conserved residues cluster in regions that we predict to have a functional role (Figure S7H and Figure S7I). This emphasizes the functional conservation between the yeast and mammalian systems and supports the similar physiological role in the eukaryotic cell we describe above. For instance, the mutation D700N in hNPC1 leads to a severe form of NPC, and we can now rationalize this with its proposed role at the proton-relay site (Garver et
395 al., 2010). The observed structural and mechanistic conservation also rationalize why yeast NCR1 can rescue Chinese hamster ovary cells defective for NPC1 (Malathi et al., 2004).

In conclusion, we demonstrate that essential components of the yeast sterol homeostasis system are similar to the human system. Based on our results, we propose a coherent general mechanism for the integration of sterols into the membrane by the NPC family which has pinpointed several previously undescribed regions of functional
400 interest. Our work establishes a framework for future research, helping the field to address this key eukaryotic sterol integration system in a rational manner.

Acknowledgements

The authors acknowledge beamlines I24, I04-1 and I04 at the Diamond Light Source, where X-ray data were collected, and Max IV Laboratory, DESY-PETRA III, ESRF and the Swiss Light Source for screening. Final EM
405 data were collected at the Astbury Biostructure Laboratory, supported through the Wellcome Trust
(108466/Z/15/Z). Grid screening and data collections was supported by iNEXT (5538) and done at the eBIC
facility at Diamond Light Source and the Core Facility for Integrated Microscopy, Faculty of Health and Medical
Sciences, University of Copenhagen, and the Aarhus University Cryo-EM facility. The Villum Center for
Bioanalytical Sciences is acknowledged for confocal microscopy instrumentation support. Anita Lunding (BMB,
410 SDU) is thanked for technical assistance. Research was supported by funding from the European Research
Council (grant agreement No. 637372), the Danish Council for Independent Research (grant agreement No.
DFF-4002-0052), the Carlsberg Foundation (CF17-0180) and an AIAS fellowship to B.P.P. Wellcome Trust ISSF
fellowship to S.R. and the Danish Council for Independent Research (grant agreement No. DFF - 7014-00054) to
D.W.

415

Author Contributions

M.W. did protein purification, crystallization experiments and determined the structures, binding and transfer
assays with radio-labeled ligands and analyzed the data. R.T.K. did protein purification, initial crystallization
experiments, cryo-EM samples preparation, cryo-EM data collection and EM data analysis. M.S. did FRET
420 binding and transfer experiments, M.S. and K.T. established and carried out sterol in vivo transport assays. S.R.
did cryo-EM data collection and cryo-EM data analysis. S.M. designed experiments related to cryo-EM and the
data. D.W. designed experiments related to FRET binding and transfer and to sterol trafficking in living yeast
cells and analyzed the data. B.P.P. initiated and supervised the project, designed experiments, and analyzed the
data. M.W., D.W. and B.P.P. wrote the manuscript. All authors participated in manuscript editing and discussion.

425

Declaration of Interests

The authors declare no competing interests.

430 **Main figure titles and legends**

Figure 1. Crystal structures of NPC2

(A) Sterol-free NPC2 (rainbow) forms a seven stranded beta sandwich with two disulfide bridges (yellow), binding cavity (blue) and internal hydrophobic residues shown.

435 (B) Sterol-bound NPC2 (orange) overlaid on the sterol-free NPC2 (gray). Ergosterol (purple) binds at the end of the hydrophobic binding cavity.

(C) Hydrophobic binding site with ergosterol and residues comprising the binding site, with ergosterol FoFc omit map at 3 sigma (green).

(D) Bovine NPC2 with binding cavity (blue) and internal hydrophobic residues shown (orientation as panel A).

(E) Comparison of yeast NPC2 and bovine NPC2 binding cavities.

440 See also Figure S2 and Table S1.

Figure 2. Sterol affinity of NPC2 and NTD and sterol transfer assays

(A) FRET signal shows NPC2 binds Dehydroergosterol (DHE) with a $K_d = 121 \pm 75$ nM. Data points show mean \pm SEM of four ($n = 4$) independent experiments.

445 (B) NPC2 binds radioactive cholesterol with a $K_d = 591 \pm 123$ nM. Data points show mean \pm SD of four ($n = 4$) independent experiments.

(C) NPC2 competition assay. *, $P \leq 0.05$; **, $P \leq 0.01$; ***, $P \leq 0.001$ and ****, $P \leq 0.0001$ by Student's t test. Data for all radiolabeled binding assays are mean \pm SD of five ($n = 5$) independent experiments.

450 (D) FRET signal shows NTD binds Dehydroergosterol (DHE) with a $K_d = 483 \pm 83$ nM. Data points show mean \pm SEM of three ($n = 3$) independent experiments.

(E) NTD binds radioactive cholesterol with a $K_d = 675 \pm 210$ nM. Data points show mean \pm SD of four ($n = 4$) independent experiments.

(F) NTD competition assay. *, $P \leq 0.05$; **, $P \leq 0.01$; ***, $P \leq 0.001$ and ****, $P \leq 0.0001$ by Student's t test. Data for all radiolabeled binding assays are mean \pm SD of five ($n = 5$) independent experiments.

455 (G) FRET-based transfer assay of DHE from NTD to NPC2 (full line) and from NPC2 to NTD (dashed line). Data points show mean \pm SEM of three ($n = 3$) independent experiments.

(H) Transfer assay with his-tagged NPC2 as donor and untagged NTD (dotted line) or untagged NPC2 (full line) as acceptor. Data points show mean \pm SD of five ($n = 5$) independent experiments.

460 (I) Transfer assay with his-tagged NTD as donor and untagged NTD (full line) or untagged NPC2 (dotted line) as acceptor. Data points show mean \pm SD of five ($n = 5$) independent experiments.

(J) Transfer assay with his-tagged NPC2 as donor and wild type or mutated NCR1 as acceptor. Data points show mean \pm SD of three ($n = 3$) independent experiments.

See also Figure S3.

465 **Figure 3. Crystal structure of NCR1**

(A) Structure of NCR1 bound to ergosterol (purple). NTD (blue), MLD (yellow), CTD (green cartoon), M1 (light blue), SSD (orange) and remaining TMs (sand). Insert: Membrane topology diagram of NCR1 show conserved and variable regions of MLD and CTD.

(B) Membrane view from vacuolar side with SSD sterol shelf (green). Interactions of M1 and M8 and charged residues at the pseudo two-fold (black oval) are shown. M5 and M11 loops and coupler loops are shown.

(C) Membrane view rotated 90 deg. from panel B with SSD sterol shelf (green).

(D) 2FoFc density (1.5 sigma) at the three charged pseudo two-fold residues and alignment of NCR1 (Q12200), hNPC1 (Q15118), Human Patched-1 (Q13636) and *E. coli* AcrB (P31224) of this region.

See also Figures S1, S3 and S5 and Table S1.

475

Figure 4. NCR1 tunnel with sterol

(A) NTD (blue) view with NTD loop-helix gate (orange) below MLD/CTD pseudo two-fold with glycine hinge (pink). Sterol binding pocket points towards the pseudo two-fold. Human NTD (white) is superposed on MLD/CTD. The 20 deg. rotation and 40 deg. tilt is marked with arrows.

480 (B) Transfer assay with his-tagged NPC2 as donor and wild type or mutated NCR1 as acceptor. Data points show mean \pm SD of three ($n = 3$) independent experiments.

(C) NCR1 (white cartoon) with coupler loops (green and violet), stalks (yellow), NTD loop-helix gate (teal), tunnel (red surface) and ergosterol (purple sticks).

485 (D) Possible route (red) for ergosterol through the NTD loop-helix gate (teal) from NTD (blue) to the tunnel between MLD (yellow) and CTD (green).

(E) Ergosterol (purple) with Buster FoFc omit map (2.5 sigma).

See also Figures S5 and S7 and Table S2.

Figure 5. Cryo-EM structure of NCR1 confirms new conformation

490 (A) Representative micrograph and 2D classes of NCR1.

(B) Cryo-EM reconstruction of NCR1 colored by local resolution.

(C) The crystallographic model fitted by Namdinator to the cryo-EM map.

See also Figure S5.

495 **Figure 6. Live-cell imaging of sterol transport to the yeast vacuole**

(A) Representative images of cells after 48h incubation under starvation conditions for wild-type, Δ NCR1, Δ NPC2, or wild-type cells incubated with the vacuolar proton-pump inhibitor Concanamycin A (Con. A). Bar, 5 μ m.

500 (B) Quantification of sterol enriched and fragmented vacuoles. Data shows mean \pm SEM of three or four ($n = 3$ except wild-type with $n = 4$) biological replicates. *, $P \leq 0.05$; **, $P \leq 0.01$; ***, $P \leq 0.001$ by Student's t test.*.

See also Figure S6.

Figure 7. Model of NPC family mediated sterol integration

505 In pre-loading state (top left), NTD (blue) is ready to receive a sterol. sterol loaded NPC2 docks to MLD (yellow) forming the loading complex (top right). The sterol is transferred from NPC2 to NTD. The NTD rotates so the binding pocket aligns with the tunnel, and the sterol is moved from NTD to tunnel. The sterol is transported to the SSD, possibly by movements generated by sequential protonation and deprotonation of the charged residues at the transmembrane pseudo two-fold (bottom). The sterol exits at the SSD shelf and
510 dissociates into the outer leaflet of the lipid bilayer.

See also Figures S5 and S7 and Table S2.

Supplemental figure titles and legends

Figure S1. Sequence alignment of *S. cerevisiae* NCR1 and *H. sapiens* hNPC1, Related to Figure 3

515 Alignment between NCR1 (accession number Q12200), and hNPC1 (accession number O15118), based on a multiple sequence alignment in Promals3D followed by small manual adjustments based on structural comparison. Conserved residues are highlighted with black. Residues that could not be modeled in the structure have a gray font. Colored tubes and arrows represent alpha-helices and beta-strands found in NTD (blue), SSD (orange), MLD (yellow), Transmembrane region (wheat) and CTD (green). Key residues are labeled below the alignment, and elements of interest above the secondary structure designation. NTD-gate is show in orange, 520 cytosolic helices in light and dark cyan, coupler loops in green and violet. Signal peptide is highlighted with a gray box. The MLD and CTD variable regions are highlighted with dashed lines. Residues of the glycine hinge and the transmembrane proton network are highlighted with pink, asparagines with observed glycosylation with green, and cysteines involved in disulfide bridges are highlighted with orange.

525 Figure S2. Sequence alignment and crystal structures of *S. cerevisiae* NPC2, Related to Figure 1

(A) Alignment between NPC2 (accession number Q12408), and hNPC2 (accession number P61916), based on a multiple sequence alignment in Promals3D followed by small manual adjustments based on structural comparison. Conserved residues are highlighted with black. Residues that could not be modeled in the structure have a gray font. Colored tubes and arrows represent alpha-helices and beta-strands. Signal peptide and pro-peptide are highlighted with gray boxes. Asparagines with observed glycosylation are highlighted with green and 530 cysteines involved in disulfide bridges are highlighted with orange.

(B) SDS-PAGE gel of the final sample for crystallization. Crystals of sterol-free NPC2. The black scale bar is 100 μm . Weighted 2FoFc density of the asymmetric unit, showing the threefold symmetry of the trimer contoured at 1.2 sigma

535 (C) Interaction between propeptide (purple) from symmetry related monomer to chain C (light orange) in sterol-free NPC2. Chain A and B does not have a similar interaction, and their propeptide cannot be resolved in the density.

(D) Crystals of sterol-bound NPC2. The black scale bar is 100 μm . Weighted 2FoFc density of the trimer formed by chain A, B and C contoured at 1.2 sigma.

540 (E) Asymmetric unit of sterol-bound NPC2 crystals containing 9 monomers, connected as 3 trimers (A-C, D-F and G-I). Five monomers have ergosterol bound (purple). The remaining four have density in the cavity that cannot be confidently modeled.

(F) Weighted FoFc density (green) with ergosterol (purple) omitted shown at 3 sigma. To the right is shown a Polder map (green) at 6.0 sigma with CC(with ligand, input)=0.84 and CC(without ligand, input)=0.56. The 545 difference in polder-map CC support a model with ligand included.

(G) Weighted FoFc density (3 sigma) in the cavity of chain A and chain H of sterol bound NPC2. The sterol of chain A was omitted before refinement and map calculation. Density in chain A show a single sterol molecule, while the density in chain H could not be confidently modeled.

550 (H) Overlay of human (dark gray) and bovine (white) NPC2 with yeast sterol bound NPC2 (rainbow). Ergosterol from the NPC2 structure is shown (purple) together with cholesterol sulphate (white and dark gray) from the human and bovine structures.

(I) There is space enough for an additional sterol in the yeast NPC2 cavity as illustrated by *in silico* modelling of an additional ergosterol into the pocket (white).

555 **Figure S3. Spectral data for DHE binding and transfer assays, Related to Figure 2**

(A) Spectral data for DHE binding to NPC2 as shown in Figure 2A. NPC2 has a characteristic peak at 305 nm, which stems primarily from Tyr residues (no Trp is present in NPC2). Binding of the naturally occurring intrinsically fluorescent ergosterol analog dehydroergosterol (DHE) leads to aromatic residue fluorescence quenching at 305 nm and additionally gives a characteristic peak at DHE's emission between 365 and 425 nm, 560 which is characteristic for Förster resonance energy transfer (FRET) from aromatic residues to DHE. Each trace is the average of 3 individual measurements and the standard error of the mean (SEM) is shown. The binding curve in Figure 2A is derived from the FRET signal at 375 nm.

(B) Spectral data for DHE binding to NTD as shown in Figure 2D. NTD has a characteristic emission at 330 nm generated primarily by Trp residues in the protein which is quenched by DHE binding while FRET leads to 565 increase in DHE emission between 365 and 425 nm. Each trace is the average of 3 individual measurements and the SEM shown. The binding curve in Figure 2D is derived from the FRET signal at 400 nm.

(C) Emission spectra of 1.0 μ M NPC2 in the absence (black line) or presence (red line) of 1.0 μ M DHE added from an ethanol stock solution as described in Methods. Spectra for background (binding buffer for black line and binding buffer with 1.0 μ M DHE for red line) were acquired separately and subtracted from the 570 measurements. The spectra show that there is no FRET from NPC2 to DHE when exciting at 295 nm.

(D) Excitation spectra of 1.0 μ M NPC2 (emission at 305 nm; black curve) and of 1.0 μ M NTD (emission at 330 nm; red curve) [both in the presence of 1 μ M DHE]. Both proteins show excitation maxima at 232 nm (from the protein backbone) and around 270-280 nm stemming from aromatic residues. However, only NTD can be 575 excited at 295 nm, where excitation of NPC2 is close to zero (blue arrows). At 295 nm Trp residues but no Phe or Tyr residues absorb, which allows for selective excitation of NTD. The inset shows the wavelength range between 270-298 nm enlarged. All spectra are selective examples from 2-4 repetitions.

(E) Spectral data for DHE transfer from NTD to NPC2 as shown in Figure 2G. NTD in Tris buffer (1.0 μ M; black line) was pre-incubated with 1.0 μ M DHE (blue line) followed by addition of 0.1 μ M (red line) or 2.0 μ M (green line) NPC2. NTD shows FRET to DHE, when excited at 295 nm, which does not excite NPC2. This

580 FRET signal decreases as function of NPC2 concentration and gave for 390 nm the transfer curve shown in Figure 2G. All spectra were corrected for the respective buffers.

(F) Spectral data for DHE transfer from NPC2 to NTD as shown in Figure 2G. 1.0 μM NPC2 in Tris buffer was pre-incubated with 1.0 μM DHE followed by addition of 0.1 μM (black line), 0.5 μM (red line), 1.0 μM (green line) or 2.0 μM (yellow line) NTD. NTD shows FRET to DHE, when excited at 295 nm, which does not excite
585 NPC2. This FRET signal increases as function of NTD concentration and gave for 390 nm the transfer curve shown in Figure 2G. All spectra were corrected for the respective buffers.

Figure S4. Crystal structure of NCR1, Related to Figure 3

(A) SDS-PAGE gel of the final sample for crystallization, and the mutants of NCR1 used for transfer assays.
590 Several additional mutants in the loop-helix and tunnel regions were expressed for biochemical assays but resulted in aggregation (data not shown). LCP crystals of NCR1. The black scale bar is 100 μm . Weighted 2FoFc density at 1.2 sigma of the asymmetric unit.

(B) Disulfides (yellow) and glycosylations (green) present in the NCR1 structure.

(C) Zoom in on the SSD shelf (red volume) surrounded by M2-M5 with an ergosterol molecule shown to scale
595 next to the structure.

(D) Superposition of MLD (yellow) and CTD (green) with the variable regions shown in full colors and the sandwich part shown in pale colors. Insert: Membrane topology diagram of NCR1 highlight conserved and variable regions of the MLD and CTD.

(E) Tilt of M1 of NCR1 (blue) compared to hNPC1 (red). The structures are superposed on the transmembrane
600 domain.

(F) The sterol binding pocket of the NTD of NCR1 (blue) next to the NTD from human NPC1 (red). The loop-helix motif is shown in orange.

Figure S5. Analysis of NCR1 structure, Related to Figure 3, Figure 4, Figure 5 and Figure 7

605 (A) Conservation of the residues in NCR1 using 94 homologous sequences as identified by ConSurf. The residues of the SSD shelf and lining the tunnel are highly conserved.

(B) Weighted FoFc omit maps (green mesh) of ergosterol (purple model) calculated with phenix and Buster shown at 2.5 sigma. The Polder map (green mesh) is contoured at 4.5 sigma with CC(with ligand, input)=0.80 and CC(without ligand, input)=0.66. The difference in polder-map CC support a model with ligand included.

610 (C) Superposition of the NCR1 Cryo-EM fitted model (blue) and the NCR1 crystal structure (white).

(D) Zoom in on the NTD (from panel C) shows no tilt, but a ~ 15 deg rotation of the NTD, with the loop-helix motif stays in the same position.

615 (E) Superposition of hNPC1 (3JFD8) to the Cryo-EM fitted model of NCR1 with a zoomed view on the NTD displays the same rotation and tilt as seen in Figure 4A. This rotation and tilt changes the relative position of the sterol binding pocket so that in hNPC1 it points towards the MLD and is further exposed to the lumen.

(F) Superposition of MLD from crystal structure NCR1 (yellow) and hNPC1 (red) with the variable regions shown in full colors and the sandwich part shown in pale colors. The loops in the variable region of hNPC1 found to interact with NPC2 in the complex structure (5KWY) does not appear conserved from hNPC1 to NCR1.

620

Figure S6. Sterol transport from the plasma membrane to the vacuole depends on NCR1/NPC2, Related to Figure 6

625 (A-B) Wild-type (A) and NCR1-deficient (B) yeast were labeled with 20 $\mu\text{g}/\text{mL}$ DHE and 1 $\mu\text{g}/\text{mL}$ FM4-64 for 22h in an anaerobic chamber at 30°C, washed and cultured without dilution under aerobic growth conditions in their original growth medium for further 0.5, 6, 24 and 48h. This procedure ensured starvation conditions throughout the whole experiment. DHE is initially, after switch to aerobic growth, found in the plasma membrane and few intracellular spots, while the sterol accumulated in lipid droplets surrounding the vacuole after 6h incubation in both cell types. Some DHE lacking the droplet marker was also found inside the vacuole. After 24h and 48h of incubation, DHE was found in lipid droplets stained with BODIPY as described in
630 Materials and Methods. Sterol-containing lipid droplets merged with the vacuole, and DHE was observed inside the vacuole lumen and along the vacuolar membrane in wild-type cells (A). In contrast, in NCR1-deficient cells, DHE accumulated at 24h and 48h in large punctate lipid droplets containing BODIPY outside and inside the vacuole, which appeared fragmented and multivesicular (B).

635 (C-D) Vacuoles stained with FM4-64 and associated with BODIPY labeled lipid droplets were imaged on a confocal microscope operating in z-sectioning modus. Individual planes being 0.3 μm apart are shown through the entire volume of the vacuoles. While the vacuole in wild-type cells (upper panel) is round and contains numerous small and weakly stained BODIPY patches, that in NCR1-deficient cells (lower panel) is multi-vesicular and contains many large lipid droplets, brightly stained with the BODIPY dye. D, vacuolar phenotypes were scored by confocal microscope from a single experiment carried out in duplicate with >30 vacuoles per
640 condition. Four sub-types were distinguished; droplets inside and at rim of round vacuole (I), lipid droplets only at rim of round vacuole (II), lipid droplets only outside of round vacuole (III) and fragmented multi-vesicular bright with multiple large lipid droplets (IV). While wild-type cells primarily had type I and II vacuoles, NCR1-deficient fibroblasts had most vacuoles of type III and IV.

645

Figure S7. Comparison of NCR1 to hNPC1, AcrB and Patched-1 and NPC disease mutations plotted, Related to Figure 4 and Figure 7

- 650 (A-E) Tunnel (red) through NCR1 (orange), AcrB (4DX5, green), Patched-1 (6DMB, yellow), hNPC1 crystal structure without NTD (5U74, purple) and hNPC1 cryo-EM structure (3JD8, purple). Below each structure is a zoom in panel of the residues implied in proton coupling with distances shorter than 3.8 Å. For AcrB, only chain B is shown as this is the conformation with the longest opening of the Porter domain tunnel/transport cavity. Compared to the eukaryotic RND tunnels, the AcrB tunnel is mirrored in AcrB along the pseudo two-fold.
- 655 (F) Alignment of the transmembrane domains of the structures listed in A-E show the residues implicated in proton coupling to all be in similar positions.
- (G) Human NPC1 (3DJ8) contain large deviations in the model, with most of the Sterol Sensing Domain having residues shifted by over 10 positions compared to the hNPC1 crystal structure (5U74). Sequence alignment to NCR1 and sequence membrane topology prediction services confirm these deviations of the model 3DJ8. In green are shown positions that agree with 5U74. Yellow regions have a frameshift of 1 residue. Orange regions have frameshifts of between 2 and 9 residues. Red regions have frameshifts of 10 to 20 residues.
- 660 (H) Missense mutations related to Niemann-Pick disease Type C plotted on NCR1, and colored by conservation: identical (red), functionally conserved (orange) and not conserved (wheat).
- (I) Same mutations as in panel H, now colored by likely interference to functional categories: protonation site
- 665 (red), pincer movement (blue), sterol pathway (orange) and stability/folding (green).

STAR Methods

KEY RESOURCES TABLE

[see separate document]

670

LEAD CONTACT AND MATERIALS AVAILABILITY

Further information and requests for resources and reagents should be directed to and will be fulfilled by the Lead Contact, Bjørn P. Pedersen (bpp@mbg.au.dk).

675 EXPERIMENTAL MODEL AND SUBJECT DETAILS

The *S. cerevisiae* expression strain DSY-5 (Gentaur) is propagated by growth in standard Yeast Extract–Peptone–Dextrose (YPD) liquid media, grown at 30° C at 150 rpm.

All strains for *in vivo* assays were generated in the BY4741 or BY4742 background. BY4741 (WT) cells were obtained from the Euroscarf culture collection (<http://www.euroscarf.de>). The CBY5147 (BY4742

680 ncr1Δ::KanMX4) and CBY5340 (BY4742 npc2Δ::KanMX4) were kindly provided by Prof. Christopher Beh, Simon Fraser University, Burnaby, Canada but originally obtained from the Open Biosystems deletion collection (<https://dharmacon.horizondiscovery.com/>).

For each experiment, cells were first grown overnight on a solid YPD agar plate containing G418 (200 µg/mL). Subsequently, single colonies of the BY4741 (WT), CBY5147 and CBY5340 strains were grown in 5 ml YPDade media (2% glucose, 2% peptone, 1% yeast extract, 0.02%

685 adenine) in a 50-ml Falcon tube at 30° C at 150 rpm, until they reached stationary phase.

METHOD DETAILS

PROTEIN EXPRESSION

Genes encoding the *Saccharomyces cerevisiae* NCR1 (Accession number Q12200), NCR1_NTD (aa 1-244) and
690 the *Saccharomyces cerevisiae* NPC2 (Accession number Q12408) were introduced into an expression construct based on p423_GAL1 (Mumberg et al., 1994) with a C-terminal purification tag containing a thrombin cleavage site and a deca-histidine tag. The NCR1, NCR1_NTD and NPC2 constructs were transformed into the *S.*

cerevisiae expression strain DSY-5 and grown in a culture vessel to high density by fed-batch and harvested after a 22 hrs induction using galactose (Lyons et al., 2016). Harvested cells were washed twice in cold water (3,300

695 g, 10 min spin) and stored at –80° C. For cell lysis, cells were thawed and re-suspended in 750 mL Lysis buffer (600 mM NaCl, 100 mM Tris pH 7.5, 1 mM PMSF), followed by 4x1 min cycles of bead-beating with 0.5 mm glass-beads. Lysed cells were spun (21,000 g, 20 min) to pellet cell debris and unlysed cells. The supernatant was spun at 20,4526 g for 2 hrs to pellet membranes. When isolating NCR1_NTD and NPC2 the supernatant was used downstream, whilst for the membrane protein NCR1 the pelleted membranes were homogenized in

700 Membrane buffer (500 mM NaCl, 50 mM Tris pH 7.5, 20% glycerol) and flash frozen in liquid nitrogen.

PROTEIN PURIFICATION

Purification of full length NCR1

705 NCR1 membranes were solubilized for 30 min in Basis Buffer (500 mM NaCl, 50 mM Tris pH 7.5, 10%
glycerol, 20 mM imidazole) with 0.6 % n-Dodecyl- β -D-Maltopyranoside (DDM) and 1.5 mg/mL iodoacetamide
at 4° C. The solubilized sample was loaded on a 5mL HisTrap HP column equilibrated in Wash Buffer (500 mM
NaCl, 50 mM Tris pH 7.5, 10% glycerol, 20 mM imidazole, 0.017% DDM). After loading the column was
washed with ~12 column volumes (CV) W70 Buffer (500 mM NaCl, 50 mM Tris pH 7.5, 10% glycerol, 70 mM
imidazole, 0.017% DDM), followed by ~9 CV of G20 buffer (200 mM NaCl, 20 mM Tris pH 7.5, 20 mM
710 imidazole, 0.05% w/v Decyl Maltose Neopentyl Glucol (DM-NG)). Finally, 5 mL of G20 buffer with 175 units
of bovine thrombin and 2000 units Endo-H was circulated over the column ON. The following day the protein
was eluted in ~5 CV of G40 buffer (200 mM NaCl, 20 mM Tris pH 7.5, 40 mM imidazole, 0.01% w/v DM-NG)
and concentrated on a 20 mL Vivaspin concentrator (100 kDa cutoff) to < 500 μ L. The sample was loaded on a
Superdex200 10/300 GL Increase column equilibrated in G-Buffer (200 mM NaCl, 20 mM Mes pH 6.5, 0.01%
715 w/v DM-NG). The composition of the G buffer was optimized through a thermostability assay (Tomasiak et al.,
2014). Peak fractions were collected and concentrated to ~500 μ L total volume before adding 20 μ L PNGase F
and incubating at 4°C overnight. The following day the sample was again loaded on a Superdex200 10/300 GL
Increase column equilibrated in G-Buffer as before. Peak fractions were pooled and concentrated to ~10 mg/mL
and stored on ice until used for crystallization trials.

720

Purification of NPC2 for crystallization

The supernatant from lysed *S. cerevisiae* cells expressing NPC2 was mixed with imidazole to a final
concentration of 20 mM and the pH was adjusted to pH 7.5 by adding Tris-HCl pH 7.5. The supernatant was
loaded on a 5 mL HisTrap HP column equilibrated in Wash Buffer (500 mM NaCl, 50 mM Tris pH 7.5, 10%
725 glycerol, 20 mM imidazole). The column was washed with ~20 CV W70 Buffer (500 mM NaCl, 50 mM Tris pH
7.5, 10% glycerol, 70 mM imidazole) followed by ~9 CV of G20 buffer (200 mM NaCl, 20 mM Tris pH 7.5, 20
mM imidazole). When crystallizing the sterol/lipid free form of NPC2 the W70 buffer also contained 0.017%
DDM to remove bound lipids/sterols. Finally, 5 mL of G20 buffer with 175 units of bovine thrombin and 2000
units Endo-H was circulated over the column ON. The protein was eluted with ~5 CV of G40 buffer (200 mM
730 NaCl, 20 mM Tris pH 7.5, 40 mM imidazole) and concentrated on a 20 mL Vivaspin concentrator (10 kDa
cutoff) to < 500 μ L. The sample was loaded on a Superdex75 10/300 GL column equilibrated in G-Buffer (200
mM NaCl, 20 mM Tris pH 7.5). Peak fractions were collected and concentrated to ~10 mg/mL.

Purification of NCR1_NTD and NPC2 for binding and transfer assays

735 For binding assays, purification of NPC2 and NCR1_NTD followed the same general protocol as in
“Purification of NPC2 for crystallization” above, but without removal of the His-tag. In brief, after washing 20
CV with a modified W70 buffer (containing 0.017% DDM to remove lipids/sterols), the protein was
immediately step eluted with 7 CV Elu500 Buffer (200 mM NaCl, 20 mM Tris pH 7.5, 500 mM imidazole), and
740 relevant fractions were pooled and buffer exchanged into G-Buffer (200 mM NaCl, 20 mM Tris pH 7.5) while
being concentrated on a 20 mL Vivaspin concentrator (10 kDa-cutoff) to < 500 μ l. The sample was loaded on a
Superdex75 10/300 GL column equilibrated in G-Buffer. Selected fractions were pooled and stored on ice until
used for assays.

STRUCTURAL DETERMINATION

745 **Crystallization and data processing of NCR1**

Lipid mix was prepared by mixing 50-75 mg Monoolein with 1,2-dioleoyl-sn-glycero-3-phosphocholine
(DOPC) in a 1:10 weight ratio. Ergosterol was solubilized in chloroform and added to the mixture to a final
concentration of 0.5% w/w. The chloroform was evaporated, and the lipid mixture heated to 42°C and mixed
with protein (3:2 w/w) using a Hamilton syringe to create the LCP. 50 nL drops of LCP plus 1 μ L screen were
750 pipetted to crystallization plates (Gryphon, Art Robins Instruments) and stored at 18°C. The final crystal
conditions were: 14-18% w/v pentaerythritol propoxylate (5/4 PO/OH), 100 mM MES pH 6.1, 87.5 mM NH₄Cl,
8-14 mM MnCl₂. One day before fishing crystals, the reservoir solution was exchanged with a similar solution
containing an additional 20% w/v pentaerythritol propoxylate (5/4 PO/OH). 10 min before fishing the trays were
transferred to 4°C and crystals fished using Dual Thickness MicroMounts from MiTiGen. Datasets were
755 collected at beamlines I04, I04-1, I24 (DLS), BioMAX (MAX IV), P14 (DESY-PETRA III) and PXI (SLS).
Data was processed and scaled with XDS (Kabsch, 2010). The phase problem was solved by Molecular
Replacement in Phaser (McCoy et al., 2007) using a chimeric Phenix sculptor (Bunkóczi and Read, 2011) model
based on hNPC1 without the NTD (pdbid: 5U73) and the isolated NTD domain (pdbid: 3GKH). This initial
NCR1 model resulted in very poor quality maps, where only few secondary elements were visible, but it could
760 be improved by a combination of Rosetta optimization in phenix.rosetta_refine (DiMaio et al., 2013) and
Molecular Dynamics based geometry optimization using MDFF (Trabuco et al., 2008) through Namdinator
(Kidmose et al., 2018). Following this optimization, the model was built in COOT (Emsley et al., 2010) guided
by 2mFo-DFc maps, Staraniso (Tickle et al., 2018 (Global Phasing Ltd.)) 2mFo-DFc maps and Feature
Enhanced Maps (Afonine et al., 2015), and refined using phenix.refine (Adams et al., 2010) and Buster (Smart et
765 al., 2012). Final refinement in phenix.refine was done with a refinement strategy of individual sites, individual
ADP, group TLS and group occupancy for the sterol ligand, against a maximum likelihood (ML) target using
reflections from the unmodified XDS dataset in the 50–3.5 Å range. The final model resulted in electron density
maps of high quality, and yielded an Rwork of 26.6% and an Rfree of 30.1% (Supplementary Table 3).

MolProbity (Chen et al., 2010) evaluation of the Ramachandran plot gave 92.1% in favored regions and 0.2% outliers.

Cryo-EM data acquisition, image processing and 3D reconstruction for NCR1

For cryo-EM, 3.5 μ L of purified NCR1 at \sim 1 mg/mL concentration were applied on glow-discharged grids (Quantifoil R1.2/1.3). The grids were blotted using a Vitrobot Mark IV (FEI) with 6 s blotting time at 100% humidity and plunge-frozen in liquid ethane. A total of 2,706 movies were recorded on a Titan Krios electron microscope (Thermo Fisher Scientific - FEI) operating at 300 kV at a magnified pixel size of 1.047 \AA . Micrographs were recorded using a K2 Summit direct electron camera (Gatan) with defocus values ranging from 1.5 μ m to 3.5 μ m. The total exposure time was 15 s resulting in an accumulated dose of \sim 60 $e^{-\text{\AA}^2}$ and a total of 24 frames per micrograph. Automatic data acquisition was carried out in EPU (Thermo Fisher Scientific - FEI). Micrographs were subjected to beam-induced motion correction using MotionCor2 (Zheng et al., 2017). CTF parameters for each micrograph were determined by CTFFIND4 (Rohou and Grigorieff, 2015). 73,423 particle images were manually picked and subjected to 2D and 3D classification within RELION 2.1 (Fernandez-Leiro and Scheres, 2017). From this step, 33,062 particles belonging to a single 3D class were selected for further processing. Focussed classification on the soluble portion of the reconstruction led to a homogeneous 20,535 particle subset. 3D auto-refinement within RELION produced a reconstruction with a global resolution of 7.2 \AA , with significant regions extending to \sim 5.6 \AA . Local resolution was determined using RELION with half map reconstructions as input maps. The crystal structure of NCR1 was fitted into the cryo-EM map by Molecular Dynamics Flexible Fitting (Trabuco et al., 2008) using Namdinator (Kidmose et al., 2018).

Crystallization and data processing of NPC2

To obtain crystals of NPC2, 200 nL reservoir + 200 nL of 10 mg/mL protein sample was set up using a Mosquito liquid handler (TTP Labtech) in a vapor diffusion setup. Crystals appeared at 19°C after 4 days using a reservoir of 200 mM Ammoniumcitrate dibasic pH 5.1, 20% PEG-3350. Crystals of the sterol-bound NPC2 appeared at 19°C after 2 days in 800 mM Lithium sulfate monohydrate, 100 mM Sodium acetate trihydrate pH 4.0, 4% PEG-200. For experimental phasing, crystals of sterol-bound NPC2 were soaked with Ta₆Br₁₂ for 1 hour before fishing. Datasets were collected at beamlines I04 (DLS), Biomax (MAX IV) and ID23-1 (ESRF). All data was processed with XDS. To solve the phase problem for NPC2, a deep search was performed using phenix.hyss (Grosse-Kunstleve and Adams, 2003) using both the sterol-bound (P6₁) and sterol-free (P6₁) dataset, resulting in a substructure solution with a total of 19 Ta sites in the sterol-bound P6₁ dataset. Initial SIRAS phases were calculated with MLphare (Winn et al., 2011) and the substructure refined using isomorphous differences (xyz, occupancy and B-factors). To improve the phases, density modification using histogram matching, solvent flattening and phase extension was done in DM (Cowtan, 1994). This resulted in initial maps of very poor

quality where however 9 monomers could be identified. A homology model made with SwissModel (Waterhouse et al., 2018) based on Lymphocyte antigen 86 (pdbid: 3T6Q) was fitted manually into the 9 monomer sites and a
805 new solvent mask was made with NcsMask (Winn et al., 2011) and used together with histogram matching in DM to improve on the phases. By fine-tuning the relative position of the monomers manually, initial NCS operators were obtained from the model with phenix.find_ncs and used to average the density with phenix.ncs_average. After rebuilding the best defined monomer, a single monomer was then used as a search model in a second Ta₆Br₁₂ soaked sterol-bound P6₂ dataset (3 monomers in the asymmetric unit) and two Ta₆Br₁₂
810 sites were found using Phaser-EP (McCoy et al., 2007). After NCS averaging, solvent flattening and histogram matching in phenix.resolve (Terwilliger, 2001) the model was rebuilt in Coot and refined in phenix.refine. The dataset was severely anisotropic and Staraniso scaling helped significantly to guide model building. After refining, a single monomer was used as a search model in Phaser on the sterol-free P6₁ dataset (3 monomers in the asymmetric unit). After this, completion of the model and final refinement in phenix.refine was done with a
815 refinement strategy of individual sites, individual ADP, torsion-angle NCS restraints, and group TLS (1 per chain) against a maximum likelihood (ML) target with reflections in the 49–2.8 Å range. The final model of sterol-free NPC2 resulted in an Rwork of 23.6% and an Rfree of 26.2%. MolProbity evaluation of the Ramachandran plot gave 96.0 % in favored regions and 0.5% outliers.

A single monomer from the final sterol-free NPC2 structure was then used as a search model in Phaser on the
820 sterol-bound P6₁ dataset (9 monomers in the asymmetric unit). Final refinement in phenix.refine was done with a refinement strategy of individual sites, torsion-angle NCS restraints, individual ADP and group TLS (1 per chain) against a maximum likelihood (ML) target with reflections in the 49–2.9 Å range. The final model resulted in an Rwork of 22.6% and an Rfree of 25.7%. MolProbity evaluation of the Ramachandran plot gave 97.0% in favored regions and 0.1% outliers.

825

Structural analysis and visualization

All structural figures were prepared using PyMOL 1.5.0.4 (The PyMOL Molecular Graphics System (Schrödinger LLC, 2012) or VMD 1.93 (Humphrey et al., 1996). Conservation of residues between homologous sequences was determined using ConSurf with default settings (Ashkenazy et al., 2016). Cavities in NPC2 were
830 characterized using CASTp with a probe radius of 1.4 Å, equivalent to the radius of water (Tian et al., 2018). The tunnel through NCR1 was identified with MOLE2.0 (Sehna et al., 2013) using default settings and a probe radius of 1.4 Å. Sequence alignments were constructed with PROMALS3D (Pei et al., 2008), followed by manually refining gaps based on the observed structure. Alignments were visualized using ALINE (Bond and Schüttelkopf, 2009).

835

BINDING AND TRANSFER ASSAYS

Radiolabeled sterol binding assay

His-tagged NPC2 or His-tagged NCR1_NTD samples were diluted into Binding Buffer (200 mM NaCl, 50 mM Mes pH 5.5, 0.004% w/v TritonX-100) and mixed in tubes at a final concentration of 75 nM with cholesterol, solubilized in Binding buffer (1600 nM cold cholesterol (from 0.1 mg/mL in ethanol stock) and 400 nM [1,2-3H(N)] cholesterol from Perkin Elmer[40-60Ci/mmol] in chloroform), at 50, 100, 150, 350, 550, 750 and 1250 nM concentration. Final volume was adjusted to 200 μ L for each reaction with Binding buffer, and triplicates were made for each concentration of cholesterol. Control triplicates were made for each of the above stated concentration of cholesterol in the absence of protein. The values obtained in the control triplicates were later subtracted from the measurements with protein present. The samples were gently vortexed and then incubated at room temperature overnight which ensured complete equilibrium of ligand binding. Next day, nickel resin was washed in Binding buffer 2 (200 mM NaCl, 80 mM Tris pH 7.5, 20 mM imidazole, 0.004% w/v TritonX-100) and 30 μ L of 50% resin slurry was transferred to each sample with 400 μ L High pH Buffer (200 mM NaCl, 80 mM Tris pH 7.5, 20 mM imidazole, 0.004% w/v TritonX-100). Following 1 hour binding, the resin was pelleted (700 g) and washed twice with 600 μ L Wash Buffer (200 mM NaCl, 20 mM Tris pH 7, 60 mM imidazole, 0.004% w/v TritonX-100). After the last wash the resin was pelleted and the protein eluted by adding 500 μ L of Elution buffer (200 mM NaCl, 20 mM Mes pH 5.5, 300 mM imidazole). The eluted protein was isolated by a final 700 g spin and moved to another tube. Scintillation liquid was added and the scintillation was measured on a Scintillation Counter (Tri-Carb 2810 TR, Perkin Elmer).

855

Radiolabeled sterol competition assay

The competition assay followed the same general protocol as in “Radiolabel sterol binding assay”. Competitors were solubilized in ethanol at 1 mg/mL and added to separate tubes with Binding Buffer (200 mM NaCl, 50 mM Mes pH 5.5, 0.004% w/v TritonX-100) to a concentration of 20 μ M. All tubes were added ethanol to ensure same total amount ethanol (1.5% final concentration of ethanol). 150 nM of His-tagged NPC2 or NTD was incubated overnight at room temperature with 1.5 μ M [1,2-3H(N)] cholesterol in Binding Buffer (200 mM NaCl, 50 mM MES pH 5.5, 0.004% w/v TritonX-100) and 7.5 μ M (5x) of either cold cholesterol, ergosterol, edelfosine, U18666A or cepharanthine followed by nickel pulldown.

865 Radiolabeled sterol transfer assay for soluble proteins NPC2 and NTD

For transfer assays, protein with and without His-tag was purified according to the two different protocols, and always with 0.017% DDM in the W70 buffer to ensure the sterol binding sites would be empty. His-tagged NPC2 or His-tagged NCR1_NTD was mixed with cholesterol and prepared as described in the “Radiolabel sterol binding assay” protocol above, but with 750 nM protein per tube and 3000nM cholesterol (2400 nM cold cholesterol and 600 nM [1,2-3H(N)] cholesterol [40-60 Ci/mmol] to obtain the sterol-donor sample. Following

elution with Elution Buffer 2 (200 mM NaCl, 20 mM Mes pH 5.5, 300 mM imidazole pH 5.5, 0.004 w/v% TritonX-100), 50 pmol sterol-donor protein was transferred to new tubes and added 25 pmol, 75 pmol and 150 pmol of sterol-acceptor protein (untagged NPC2 or NCR1_NTD) in Binding Buffer, and the total volume was adjusted to 300 μ L with Binding Buffer. The samples were incubated for 3 hrs at 4°C with gentle shaking. Nickel
875 resin was washed in High pH Buffer (200 mM NaCl, 80 mM Tris pH 7.5, 20 mM imidazole, 0.004% w/v TritonX-100), and 60 μ L of 50% resin slurry was transferred to each sample with 340 μ L High pH Buffer (200 mM NaCl, 80 mM Tris pH 7.5, 20 mM imidazole 0.004% w/v Triton X-100). Following 1 hour binding at 4°C, the resin was pelleted (700 g) and the supernatant containing the sterol-acceptor protein from each tube was removed and added scintillation liquid. The pelleted resin containing the sterol-donor protein was resuspended
880 with Elution Buffer and transferred to a new tube and added scintillation liquid. Both were measured in order to quantify the total amount of radioactivity per sample.

Radiolabeled sterol transfer assay for membrane protein NCR1 and soluble NPC2

His-tagged NPC2 was purified and loaded with radioactive cholesterol as stated earlier, but with different elution
885 buffer. After washing twice with 600 μ L Wash Buffer (200 mM NaCl, 20 mM Tris pH 7, 60 mM imidazole, 0.004% w/v TritonX-100), the sample was washed with 600 μ L Wash Buffer 2 (200 mM NaCl, 20 mM Tris pH 7, 60 mM imidazole) to remove detergent and eluted with Elution Buffer 3 (200 mM NaCl, 20 mM Mes pH 5.5, 300 mM imidazole pH 5.5). Approximately 90 pmol loaded sterol-donor protein was transferred to new tubes and added 25 pmol, 75 pmol, 150 pmol, 225 pmol or 350 pmol of sterol-acceptor protein (untagged NCR1
890 purified in 0.005% DM-NG) in Transfer Buffer (200mM, 20 mM Mes pH 5.5), then added 180 pmol his-tagged NPC2 without sterols to limit transfer to micelles, and the total volume was adjusted to 500 μ L with Transfer Buffer. The samples were incubated for 30 min at 4°C with gentle shaking. Nickel resin was washed in High pH Buffer 2 (200 mM NaCl, 10 mM Tris pH 7.5,), and 150 μ L of 50% resin slurry was transferred to each sample with 150 μ L High pH Buffer 3 (200 mM NaCl, 100 mM Tris pH 11) to increase pH to 7.5. Following 1 hour
895 binding at 4°C, the resin was pelleted (700 g) and the supernatant containing the sterol-acceptor protein from each tube was removed and added scintillation liquid. The pelleted resin containing the sterol-donor protein was resuspended with Elution Buffer and transferred to a new tube and added scintillation liquid. Both were measured in order to quantify the total amount of radioactivity per sample

900 Fluorescence-based sterol binding assay

NPC2 and NTD proteins were diluted in a modified binding buffer (100 mM NaCl, 50 mM MES pH 5.5) to a final concentration of 1 μ M in a 0.1 cm thick quartz cuvette. Intrinsic protein fluorescence was excited at 280 nm and emission was recorded in a wavelength range of 300 to 500 nm. The samples were incubated with increasing concentrations of DHE, a fluorescent analog of ergosterol, whose excitation spectrum overlaps with the emission

905 spectra of aromatic residues of both proteins. Thus, binding of DHE to NPC2 or NTD gives rise to Förster
resonance energy transfer (FRET) from Tyr and Phe of NPC2 (Figure S3A) and Trp, Tyr and Phe of NTD to
DHE (Figure S3B), respectively. The final concentration of ethanol in the cuvette for the highest DHE
concentration of 4 μM was 6%. The incubation time between each of the measurements was 15 min during
910 which shutters were closed. The measurements were done using an ISS Chronos spectrofluorometer (Urbana-
Champaign, IL). The slit width was 0.5 mm and no polarizers were used. Separate spectra were recorded for
DHE in modified binding buffer under identical conditions and subtracted from emission spectra in the presence
of each protein.

Fluorescence-based sterol transfer assay

915 NPC2 or NTD proteins were diluted in a modified binding buffer (100 mM NaCl, 50 mM MES pH 5.5) to a final
concentration of 1 μM in a 0.1 cm thick quartz cuvette. Intrinsic fluorescence of NTD was excited at 295 nm and
emission was recorded in a wavelength range of 300 to 500 nm. This excitation wavelength selectively excites
Trp, which is only present in NTD but not in NPC2. The donor protein was pre-incubated with 1.0 μM DHE, a
fluorescent analog of ergosterol, whose excitation spectrum overlaps with the emission spectrum of Trp in NTD.
920 Thus, binding of DHE to NTD but not to NPC2 gives rise to FRET under these conditions. This can be used to
advantage as transfer of DHE from NTD to NPC2 results in decrease of FRET, while transfer of DHE from
NPC2 to NTD results in increased FRET. Donor protein with bound DHE was incubated with increasing
concentrations (0.1, 0.5, 1.0 and 2.0 μM) acceptor protein, and the rise (for NPC2 to NTD) or decrease (for NTD
925 to NPC2) in FRET was measured at 390 nm and plotted as function of acceptor concentration. The incubation
time between each of the measurements was 15 min for pre-equilibration with DHE and 5 min during sterol
transfer during which shutters were closed. The measurements were done using an ISS Chronos
spectrofluorometer (Urbana-Champaign, IL). The slit width was 0.5 mm and no polarizers were used. Separate
spectra were recorded for acceptor protein in the presence of DHE but absence of the donor protein in modified
binding buffer under identical conditions. These spectra were subtracted from emission spectra of the complete
930 transfer mixture, i.e., donor and acceptor protein + DHE ligand.

IN VIVO ASSAYS

In vivo sterol transport assay

The yeast strains used in this study were BY4742 *ncr1* Δ ::KanMX4; BY4742 *npc2* Δ ::KanMX4 and
935 BY4741(WT). Yeast strains were grown in YPDade media (2% glucose, 2% peptone, 1% yeast extract, 0.02%
adenine) overnight to reach an OD600 of 28. Cells were then washed three times with sterile water and diluted to
a final concentration of 0.1 OD600 in YPDade media containing 0.1 $\mu\text{g/mL}$ of FM4-64 dye and 0.1% Tween 80
with 20 $\mu\text{g/mL}$ DHE. The yeast strains were incubated for 22h with these probes in an oxygen-depleted culture

chamber at 30°C to ensure anaerobic conditions and thereby sterol uptake. Subsequently, cells were washed
940 three times with PBS. Cells were transferred into media from the first day of growth and cultured under aerobic
conditions for 0.5h; 6h; 24h or 48h. Before imaging, cells were prepared in a small aliquot to final concentration
of 1.0 OD600 and incubated for 3min with BODIPY 493/503 (0.5 µg/mL) to stain lipid droplets. Cells were
washed and imaged. In some experiments, 3 µM Concanamycin A was added in the last 24h before staining lipid
945 droplets and imaging. Wide-field microscopy was carried out on a Leica DMIRBE microscope with a 63x 1.4
NA oil immersion objective (Leica Lasertechnik GmbH) with a Lambda SC smart shutter (Sutter Instrument
Company) as illumination control. Images were acquired with an Andor Ixon blue EMCCD camera at -75°C.
DHE was imaged in the UV using a specially designated filter cube (325-nm (20-nm bandpass) excitation filter,
365-nm dichromatic mirror and 405-nm (40-nm bandpass) emission). BODIPY493/503 was imaged using a
fluorescein filter cube (470-nm [20-nm bandpass] excitation filter, 510-nm longpass dichromatic filter and 537-
950 nm [23-nm bandpass] emission filter). FM4-64 was imaged using a standard rhodamine filter set (535-nm [50-
nm bandpass] excitation filter, 565-nm longpass dichromatic filter and 610-nm [75-nm bandpass] emission filter).
In case of DHE stacks of 25 images were acquired with 100 msec acquisition time, while for the other probes
single acquisitions were used. Correction for chromatic aberration between the UV channel and the red and
green channels was carried out as described previously (Wüstner and Faergeman, 2008). Background and signal
955 crossover was independently assessed in unstained or single-labeled samples, respectively. Confocal section
images were acquired using a Leica SP8 confocal microscope with a 63x oil objective (NA=1.4) and equipped
with a white light laser (WLL) tunable in the range of 470-700 nm. Fluorescence signals of BODIPY493/503
(WLL excitation at 488nm, emission at 506-527nm) and of FM4-64 (WLL excitation at 530nm, emission at 555-
644nm) were collected with a hybrid detector.

960

QUANTIFICATION AND STATISTICAL ANALYSIS

Data from binding and transfer assays were analyzed with either Graph Pad Prism 7 (GraphPad Software Inc.,
San Diego, CA) or SigmaPlot (Systat Software Inc., San José, CA). All experiments were performed at least in
triplicate. The n for each specific experiment is listed in the relevant figure legend.

965 For the radiolabeled binding assays, in order to account for the nonspecific binding, an average of the values
without protein present were subtracted all data points. A nonlinear regression of a hyperbolic binding model
($Y=B_{\max} \cdot X / (K_D + X)$) curve was fitted to the data according to:

$$f = B_{\max} \cdot [L] / (K_D + [L]) \quad (1)$$

970

Here, B_{\max} is the maximal signal at ligand saturation and $[L]$ is the concentration of the ligand. This model
assumes that protein concentration is significantly lower than the K_D , such that the non-bound ligand

approximates the total ligand concentration, [L]. This assumption was met in the radiolabel binding assay.

975 Before fitting, the in order to calculate a Bmax and Kd, and the data was normalized to B_{max} . For competition assays, the data was normalized to cholesterol binding without any competition. Statistical significance was calculated using Student's *t*-test.

In the transfer assays, the amount of transferred cholesterol divided by the total amount of sterol per tube was plotted as a function of acceptor protein. In order to account for the natural release of cholesterol, an average of transfer to buffer-only was subtracted all data points.

980 Binding of DHE either protein was measured by fluorescence spectroscopy after subtracting spectra of the respective DHE concentration in buffer only. Determination of dissociation constants (i.e., K_D values) was carried out using the full analytical solution of the one-site binding model for the fractional saturation, f , according to:

$$\frac{[RL]}{[R]} = \frac{P_T + K_D + [L] - \sqrt{(P_T + K_D + [L])^2 - 4 \cdot P_T \cdot [L]}}{2 \cdot P_T} = f \quad (2)$$

985 Where [RL] is the NPC2- or NTD/ligand complex, [R] is the total concentration of NPC2 or NTD, P_T is the total protein concentration and [L] is the concentration of the ligand. This model had to be invoked, since the FRET assay required higher protein concentrations, such that the approximation of non-bound ligand being close to equal the total ligand concentration, [L] does not hold anymore. Before fitting to Eq. 2, all fluorescence measurements were normalized according to

$$f = \frac{F_{[L]} - F_{[L_0]}}{F_{[min]} - F_{[L_0]}} \quad (3)$$

990

Here $F_{[L]}$ is the buffer-corrected fluorescence intensity at the given ligand concentration, $F_{[L_0]}$ is the fluorescence of the free protein i.e. [L]=0 and $F_{[min]}$ is the minimum protein intensity in the presence of saturating ligand concentration. This data was fitted to Eq. 2 to obtain an estimate for the K_D value under each condition.

995 All image analysis was carried out in ImageJ (Schneider et al., 2012). Images acquired in all three channels (UV channel for DHE; green for BODIPY and red channel for FM4-64) were deconvolved by 30 iterations of a 2D-version of the Richardson Lucy algorithm with a synthetic point spread function, as implemented in the ImageJ plugin DeconvolutionLab (Griffa et al., 2010). The contribution of background and autofluorescence in DHE images was first assessed by bleach rate imaging, as described previously (Kohut et al., 2011; Solanko et al., 2018). Correction for these factors and thereby isolation of DHE intensity was achieved by calculating the
1000 standard deviation at each pixel along the bleach stack. DHE images were subsequently deconvolved as described above. For background correction of the green and red channel images, the corresponding routine in DeconvolutionLab was used. After processing, images of all three channels were spatially aligned to correct for residual chromatic lateral shifts of 1-2 pixels in both directions, and color RGB stacks were generated. For

phenotype scoring, regions of interest (ROIs) of 8x8 μm were generated for 40 to 60 cells per RGB stack, and
1005 automatically arranged in montages of the separate channels. All images for a given channel were processed
identically and automatically by employing batch processing and self-programmed Macros in ImageJ. Results of
image-based screens on sterol disposition in vacuoles were imported into SigmaPlot (Systat Inc), and the mean
values of 6 to 8 images with 40 to 100 cells per image were calculated for three independent experiments per
condition, except wild-type condition which had four independent experiments. The total number of analyzed
1010 cells were 1126 (wt), 1400 (ΔNCR1), 1807 (ΔNPC2) and 1238 (wt+Con-A). This data was tested for normality
using a Shapiro Wilk test and for equal variance using a Brown-Forsythe test, and both tests were passed for
each condition. Statistical significances of differences between the groups were assessed using a Student's t-test,
and significance levels are shown in Figure 6B.

1015 **DATA AND SOFTWARE AVAILABILITY**

Data Resources

The atomic coordinates and structure factors have been deposited in the Protein Data Bank with the accession
code 6R4L for NCR1, and 6R4M for sterol-free NPC2(crystal structure), and 6R4N for sterol-bound NPC2. The
7.2 Å EM map for NCR1 have been deposited in EMDB with accession code EMD-4771.

1020 **Supplemental Excel table titles and legends**

Table S1. Statistics for crystallographic data collection and structure refinement, Related to Figure 1 and Figure 3.

1025 **Table S2. Niemann-Pick Disease type C missense mutations identified in literature, Related to Figure 4 and Figure 7**

References

- Adams, P.D., Afonine, P.V., Bunkóczi, G., Chen, V.B., Davis, I.W., Echols, N., Headd, J.J., Hung, L.-W., Kapral, G.J., Grosse-Kunstleve, R.W., et al. (2010). PHENIX: a comprehensive Python-based system for macromolecular structure solution. *Acta Crystallographica Section D Biological Crystallography* *66*, 213–221.
- Adebali, O., Reznik, A.O., Ory, D.S., and Zhulin, I.B. (2016). Establishing the precise evolutionary history of a gene improves prediction of disease-causing missense mutations. *Genet Med* *18*, 1029–1036.
- Afonine, P.V., Moriarty, N.W., Mustyakimov, M., Sobolev, O.V., Terwilliger, T.C., Turk, D., Urzhumtsev, A., and Adams, P.D. (2015). FEM: feature-enhanced map. *Acta Crystallogr. D Biol. Crystallogr.* *71*, 646–666.
- Ashkenazy, H., Abadi, S., Martz, E., Chay, O., Mayrose, I., Pupko, T., and Ben-Tal, N. (2016). ConSurf 2016: an improved methodology to estimate and visualize evolutionary conservation in macromolecules. *Nucleic Acids Res* *44*, W344–W350.
- Berger, A.C., Hanson, P.K., Wylie Nichols, J., and Corbett, A.H. (2005a). A yeast model system for functional analysis of the Niemann-Pick type C protein 1 homolog, Ncr1p. *Traffic* *6*, 907–917.
- Berger, A.C., Vanderford, T.H., Gernert, K.M., Nichols, J.W., Faundez, V., and Corbett, A.H. (2005b). *Saccharomyces cerevisiae* Npc2p is a functionally conserved homologue of the human Niemann-Pick disease type C 2 protein, hNPC2. *Eukaryotic Cell* *4*, 1851–1862.
- Bidet, M., Tomico, A., Martin, P., Guizouarn, H., Mollat, P., and Mus-Veteau, I. (2012). The Hedgehog receptor patched functions in multidrug transport and chemotherapy resistance. *Mol. Cancer Res.* *10*, 1496–1508.
- Bond, C.S., and Schüttelkopf, A.W. (2009). ALINE: a WYSIWYG protein-sequence alignment editor for publication-quality alignments. *Acta Crystallographica Section D Biological Crystallography* *65*, 510–512.
- Buch-Pedersen, M.J., Pedersen, B.P., Veierskov, B., Nissen, P., and Palmgren, M.G. (2009). Protons and how they are transported by proton pumps. *Pflugers Arch* *457*, 573–579.
- Bunkóczi, G., and Read, R.J. (2011). Improvement of molecular-replacement models with Sculptor. *Acta Crystallogr. D Biol. Crystallogr.* *67*, 303–312.
- Carette, J.E., Raaben, M., Wong, A.C., Herbert, A.S., Obernosterer, G., Mulherkar, N., Kuehne, A.I., Kranzusch, P.J., Griffin, A.M., Ruthel, G., et al. (2011). Ebola virus entry requires the cholesterol transporter Niemann-Pick C1. *Nature* *477*, 340–343.
- Carstea, E.D., Morris, J.A., Coleman, K.G., Loftus, S.K., Zhang, D., Cummings, C., Gu, J., Rosenfeld, M.A., Pavan, W.J., Krizman, D.B., et al. (1997). Niemann-Pick C1 disease gene: homology to mediators of cholesterol homeostasis. *Science* *277*, 228–231.

Chen, V.B., Arendall, W.B., 3rd, Headd, J.J., Keedy, D.A., Immormino, R.M., Kapral, G.J., Murray, L.W., Richardson, J.S., and Richardson, D.C. (2010). MolProbity: all-atom structure validation for macromolecular crystallography. *Acta Crystallogr. D Biol. Crystallogr.* *66*, 12–21.

Côté, M., Misasi, J., Ren, T., Bruchez, A., Lee, K., Filone, C.M., Hensley, L., Li, Q., Ory, D., Chandran, K., et al. (2011). Small molecule inhibitors reveal Niemann-Pick C1 is essential for Ebola virus infection. *Nature* *477*, 344–348.

Cowtan, K. (1994). “dm”: An automated procedure for phase improvement by density modification. *CCP4 Newsletter in Protein Crystallography* *31*, 34–38.

Davies, J.P., and Ioannou, Y.A. (2000). Topological analysis of Niemann-Pick C1 protein reveals that the membrane orientation of the putative sterol-sensing domain is identical to those of 3-hydroxy-3-methylglutaryl-CoA reductase and sterol regulatory element binding protein cleavage-activating protein. *J. Biol. Chem.* *275*, 24367–24374.

Davies, J.P., Chen, F.W., and Ioannou, Y.A. (2000). Transmembrane molecular pump activity of Niemann-Pick C1 protein. *Science* *290*, 2295–2298.

Deffieu, M.S., and Pfeffer, S.R. (2011). Niemann-Pick type C 1 function requires luminal domain residues that mediate cholesterol-dependent NPC2 binding. *Proc. Natl. Acad. Sci. U.S.A.* *108*, 18932–18936.

DiMaio, F., Echols, N., Headd, J.J., Terwilliger, T.C., Adams, P.D., and Baker, D. (2013). Improved low-resolution crystallographic refinement with Phenix and Rosetta. *Nat. Methods* *10*, 1102–1104.

Du, X., Kumar, J., Ferguson, C., Schulz, T.A., Ong, Y.S., Hong, W., Prinz, W.A., Parton, R.G., Brown, A.J., and Yang, H. (2011). A role for oxysterol-binding protein-related protein 5 in endosomal cholesterol trafficking. *J. Cell Biol.* *192*, 121–135.

Emsley, P., Lohkamp, B., Scott, W.G., and Cowtan, K. (2010). Features and development of Coot. *Acta Crystallogr. D Biol. Crystallogr.* *66*, 486–501.

Enkavi, G., Mikkolainen, H., Güngör, B., Ikonen, E., and Vattulainen, I. (2017). Concerted regulation of npc2 binding to endosomal/lysosomal membranes by bis(monoacylglycerol)phosphate and sphingomyelin. *PLoS Comput. Biol.* *13*, e1005831.

Fernandez-Leiro, R., and Scheres, S.H.W. (2017). A pipeline approach to single-particle processing in RELION. *Acta Crystallogr D Struct Biol* *73*, 496–502.

Friedland, N., Liou, H.-L., Lobel, P., and Stock, A.M. (2003). Structure of a cholesterol-binding protein deficient in Niemann-Pick type C2 disease. *Proc. Natl. Acad. Sci. U.S.A.* *100*, 2512–2517.

Furuchi, T., Aikawa, K., Arai, H., and Inoue, K. (1993). Bafilomycin A1, a specific inhibitor of vacuolar-type H(+)-ATPase, blocks lysosomal cholesterol trafficking in macrophages. *J. Biol. Chem.* *268*, 27345–27348.

- Garver, W.S., Jelinek, D., Meaney, F.J., Flynn, J., Pettit, K.M., Shepherd, G., Heidenreich, R.A., Vockley, C.M.W., Castro, G., and Francis, G.A. (2010). The National Niemann-Pick Type C1 Disease Database: correlation of lipid profiles, mutations, and biochemical phenotypes. *J. Lipid Res.* *51*, 406–415.
- Griffa, A., Garin, N., and Sage, D. (2010). Comparison of Deconvolution Software . A user point of view. *G.I.T. Imaging and Microscopy* *3*, 41–43.
- Gong, X., Qian, H., Zhou, X., Wu, J., Wan, T., Cao, P., Huang, W., Zhao, X., Wang, X., Wang, P., et al. (2016). Structural Insights into the Niemann-Pick C1 (NPC1)-Mediated Cholesterol Transfer and Ebola Infection. *Cell* *165*, 1467–1478.
- Gong, X., Qian, H., Cao, P., Zhao, X., Zhou, Q., Lei, J., and Yan, N. (2018). Structural basis for the recognition of Sonic Hedgehog by human Patched1. *Science* *361*.
- Grosse-Kunstleve, R.W., and Adams, P.D. (2003). Substructure search procedures for macromolecular structures. *Acta Crystallogr. D Biol. Crystallogr.* *59*, 1966–1973.
- Hua, X., Nohturfft, A., Goldstein, J.L., and Brown, M.S. (1996). Sterol resistance in CHO cells traced to point mutation in SREBP cleavage-activating protein. *Cell* *87*, 415–426.
- Humphrey, W., Dalke, A., and Schulten, K. (1996). VMD: visual molecular dynamics. *J Mol Graph* *14*, 33–38, 27–28.
- Infante, R.E., Wang, M.L., Radhakrishnan, A., Kwon, H.J., Brown, M.S., and Goldstein, J.L. (2008). NPC2 facilitates bidirectional transfer of cholesterol between NPC1 and lipid bilayers, a step in cholesterol egress from lysosomes. *Proc. Natl. Acad. Sci. U.S.A.* *105*, 15287–15292.
- Jacquier, N., and Schneiter, R. (2012). Mechanisms of sterol uptake and transport in yeast. *J. Steroid Biochem. Mol. Biol.* *129*, 70–78.
- Kabsch, W. (2010). XDS. *Acta Crystallographica Section D Biological Crystallography* *66*, 125–132.
- Kidmose, R.T., Juhl, J., Nissen, P., Boesen, T., Karlsen, J.L., and Pedersen, B.P. (2019). Namdinator - Automatic Molecular Dynamics flexible fitting of structural models into cryo-EM and crystallography experimental maps. *IUCrJ* *6*, 526-531.
- Kohut, P., Wüstner, D., Hronska, L., Kuchler, K., Hapala, I., and Valachovic, M. (2011). The role of ABC proteins Aus1p and Pdr11p in the uptake of external sterols in yeast: dehydroergosterol fluorescence study. *Biochem. Biophys. Res. Commun.* *404*, 233–238.
- Kumar, N., Su, C.-C., Chou, T.-H., Radhakrishnan, A., Delmar, J.A., Rajashankar, K.R., and Yu, E.W. (2017). Crystal structures of the *Burkholderia multivorans* hopanoid transporter HpnN. *Proc. Natl. Acad. Sci. U.S.A.* *114*, 6557–6562.

- Kuwabara, P.E., and Labouesse, M. (2002). The sterol-sensing domain: multiple families, a unique role? *Trends Genet.* *18*, 193–201.
- Kwon, H.J., Abi-Mosleh, L., Wang, M.L., Deisenhofer, J., Goldstein, J.L., Brown, M.S., and Infante, R.E. (2009). Structure of N-terminal domain of NPC1 reveals distinct subdomains for binding and transfer of cholesterol. *Cell* *137*, 1213–1224.
- Li, X., Wang, J., Coutavas, E., Shi, H., Hao, Q., and Blobel, G. (2016a). Structure of human Niemann-Pick C1 protein. *Proc. Natl. Acad. Sci. U.S.A.*
- Li, X., Saha, P., Li, J., Blobel, G., and Pfeffer, S.R. (2016b). Clues to the mechanism of cholesterol transfer from the structure of NPC1 middle luminal domain bound to NPC2. *Proc. Natl. Acad. Sci. U.S.A.* *113*, 10079–10084.
- Loftus, S.K., Erickson, R.P., Walkley, S.U., Bryant, M.A., Incao, A., Heidenreich, R.A., and Pavan, W.J. (2002). Rescue of neurodegeneration in Niemann-Pick C mice by a prion-promoter-driven *Npc1* cDNA transgene. *Hum. Mol. Genet.* *11*, 3107–3114.
- Lu, F., Liang, Q., Abi-Mosleh, L., Das, A., De Brabander, J.K., Goldstein, J.L., and Brown, M.S. (2015). Identification of NPC1 as the target of U18666A, an inhibitor of lysosomal cholesterol export and Ebola infection. *Elife* *4*.
- Lyons, J.A., Shahsavari, A., Paulsen, P.A., Pedersen, B.P., and Nissen, P. (2016). Expression strategies for structural studies of eukaryotic membrane proteins. *Curr. Opin. Struct. Biol.* *38*, 137–144.
- Malathi, K., Higaki, K., Tinkelenberg, A.H., Balderes, D.A., Almanzar-Paramio, D., Wilcox, L.J., Erdeniz, N., Redican, F., Padamsee, M., Liu, Y., et al. (2004). Mutagenesis of the putative sterol-sensing domain of yeast Niemann Pick C-related protein reveals a primordial role in subcellular sphingolipid distribution. *J. Cell Biol.* *164*, 547–556.
- McCoy, A.J., Grosse-Kunstleve, R.W., Adams, P.D., Winn, M.D., Storoni, L.C., and Read, R.J. (2007). *Phaser* crystallographic software. *J Appl Cryst* *40*, 658–674.
- Mumberg, D., Müller, R., and Funk, M. (1994). Regulatable promoters of *Saccharomyces cerevisiae*: comparison of transcriptional activity and their use for heterologous expression. *Nucleic Acids Res.* *22*, 5767–5768.
- Munkacsy, A.B., Chen, F.W., Brinkman, M.A., Higaki, K., Gutiérrez, G.D., Chaudhari, J., Layer, J.V., Tong, A., Bard, M., Boone, C., et al. (2011). An “exacerbate-reverse” strategy in yeast identifies histone deacetylase inhibition as a correction for cholesterol and sphingolipid transport defects in human Niemann-Pick type C disease. *J. Biol. Chem.* *286*, 23842–23851.
- Naureckiene, S., Sleat, D.E., Lackland, H., Fensom, A., Vanier, M.T., Wattiaux, R., Jadot, M., and Lobel, P. (2000). Identification of HE1 as the second gene of Niemann-Pick C disease. *Science* *290*, 2298–2301.

Neiss, W.F. (1984). A coat of glycoconjugates on the inner surface of the lysosomal membrane in the rat kidney. *Histochemistry* *80*, 603–608.

Ohgami, N., Ko, D.C., Thomas, M., Scott, M.P., Chang, C.C.Y., and Chang, T.-Y. (2004). Binding between the Niemann–Pick C1 protein and a photoactivatable cholesterol analog requires a functional sterol-sensing domain. *Proc Natl Acad Sci U S A* *101*, 12473–12478.

Ohgane, K., Karaki, F., Dodo, K., and Hashimoto, Y. (2013). Discovery of oxysterol-derived pharmacological chaperones for NPC1: implication for the existence of second sterol-binding site. *Chem. Biol.* *20*, 391–402.

Ouimet, M., Franklin, V., Mak, E., Liao, X., Tabas, I., and Marcel, Y.L. (2011). Autophagy regulates cholesterol efflux from macrophage foam cells via lysosomal acid lipase. *Cell Metab.* *13*, 655–667.

Pei, J., Kim, B.-H., and Grishin, N.V. (2008). PROMALS3D: a tool for multiple protein sequence and structure alignments. *Nucleic Acids Res.* *36*, 2295–2300.

Pentchev, P.G. (2004). Niemann-Pick C research from mouse to gene. *Biochim. Biophys. Acta* *1685*, 3–7.

Pfeffer, S.R. (2019). NPC intracellular cholesterol transporter 1 (NPC1)-mediated cholesterol export from lysosomes. *J. Biol. Chem.* *294*, 1706–1709.

Qi, X., Schmiede, P., Coutavas, E., Wang, J., and Li, X. (2018a). Structures of human Patched and its complex with native palmitoylated sonic hedgehog. *Nature* *560*, 128–132.

Qi, X., Schmiede, P., Coutavas, E., and Li, X. (2018b). Two Patched molecules engage distinct sites on Hedgehog yielding a signaling-competent complex. *Science* *362*.

Rohou, A., and Grigorieff, N. (2015). CTFFIND4: Fast and accurate defocus estimation from electron micrographs. *J. Struct. Biol.* *192*, 216–221.

Schneider, C.A., Rasband, W.S., and Eliceiri, K.W. (2012). NIH Image to ImageJ: 25 years of image analysis. *Nat. Methods* *9*, 671–675.

Schulze, H., Kolter, T., and Sandhoff, K. (2009). Principles of lysosomal membrane degradation: Cellular topology and biochemistry of lysosomal lipid degradation. *Biochim. Biophys. Acta* *1793*, 674–683.

Sehna, D., Svobodová Vařeková, R., Berka, K., Pravda, L., Navrátilová, V., Banáš, P., Ionescu, C.-M., Otyepka, M., and Koča, J. (2013). MOLE 2.0: advanced approach for analysis of biomacromolecular channels. *J. Cheminform* *5*, 39.

Sarkar, S., Carroll, B., Buganim, Y., Maetzel, D., Ng, A.H.M., Cassady, J.P., Cohen, M.A., Chakraborty, S., Wang, H., Spooner, E., et al. (2013). Impaired autophagy in the lipid-storage disorder Niemann-Pick type C1 disease. *Cell Rep* *5*, 1302–1315.

Smart, O.S., Womack, T.O., Flensburg, C., Keller, P., Paciorek, W., Sharff, A., Vonrhein, C., and Bricogne, G. (2012). Exploiting structure similarity in refinement: automated NCS and target-structure restraints in BUSTER. *Acta Crystallogr. D Biol. Crystallogr.* *68*, 368–380.

Solanko, L.M., Sullivan, D.P., Sere, Y.Y., Szomek, M., Lunding, A., Solanko, K.A., Pizovic, A., Stanchev, L.D., Pomorski, T.G., Menon, A.K., et al. (2018). Ergosterol is mainly located in the cytoplasmic leaflet of the yeast plasma membrane. *Traffic* *19*, 198–214.

Su, C.-C., Klenotic, P.A., Bolla, J.R., Purdy, G.E., Robinson, C.V., and Yu, E.W. (2019). MmpL3 is a lipid transporter that binds trehalose monomycolate and phosphatidylethanolamine. *Proc. Natl. Acad. Sci. U.S.A.* *116*, 11241–11246.

Terwilliger, T.C. (2001). Maximum-likelihood density modification using pattern recognition of structural motifs. *Acta Cryst D* *57*, 1755–1762.

Tian, W., Chen, C., Lei, X., Zhao, J., and Liang, J. (2018). CASTp 3.0: computed atlas of surface topography of proteins. *Nucleic Acids Res.* *46*, W363–W367.

Tomasiak, T.M., Pedersen, B.P., Chaudhary, S., Rodriguez, A., Colmanares, Y.R., Roe-Zurz, Z., Thamminana, S., Tessema, M., and Stroud, R.M. (2014). General qPCR and Plate Reader Methods for Rapid Optimization of Membrane Protein Purification and Crystallization Using Thermostability Assays. *Curr Protoc Protein Sci* *77*, 29.11.1-14.

Trabuco, L.G., Villa, E., Mitra, K., Frank, J., and Schulten, K. (2008). Flexible fitting of atomic structures into electron microscopy maps using molecular dynamics. *Structure* *16*, 673–683.

Trinh, M.N., Brown, M.S., Seemann, J., Goldstein, J.L., and Lu, F. (2018). Lysosomal cholesterol export reconstituted from fragments of Niemann-Pick C1. *Elife* *7*.

Tsuji, T., Fujimoto, M., Tatematsu, T., Cheng, J., Orii, M., Takatori, S., and Fujimoto, T. (2017). Niemann-Pick type C proteins promote microautophagy by expanding raft-like membrane domains in the yeast vacuole. *Elife* *6*.

Wang, H., Shi, Y., Song, J., Qi, J., Lu, G., Yan, J., and Gao, G.F. (2016). Ebola Viral Glycoprotein Bound to Its Endosomal Receptor Niemann-Pick C1. *Cell* *164*, 258–268.

Wang, M.L., Motamed, M., Infante, R.E., Abi-Mosleh, L., Kwon, H.J., Brown, M.S., and Goldstein, J.L. (2010). Identification of surface residues on Niemann-Pick C2 essential for hydrophobic handoff of cholesterol to NPC1 in lysosomes. *Cell Metab.* *12*, 166–173.

Waterhouse, A., Bertoni, M., Bienert, S., Studer, G., Tauriello, G., Gumienny, R., Heer, F.T., de Beer, T.A.P., Rempfer, C., Bordoli, L., et al. (2018). SWISS-MODEL: homology modelling of protein structures and complexes. *Nucleic Acids Res.* *46*, W296–W303.

Winn, M.D., Ballard, C.C., Cowtan, K.D., Dodson, E.J., Emsley, P., Evans, P.R., Keegan, R.M., Krissinel, E.B., Leslie, A.G.W., McCoy, A., et al. (2011). Overview of the CCP4 suite and current developments. *Acta Crystallographica Section D Biological Crystallography* 67, 235–242.

Wüstner, D., and Faergeman, N.J. (2008). Chromatic aberration correction and deconvolution for UV sensitive imaging of fluorescent sterols in cytoplasmic lipid droplets. *Cytometry A* 73, 727–744.

Xu, S., Benoff, B., Liou, H.-L., Lobel, P., and Stock, A.M. (2007). Structural basis of sterol binding by NPC2, a lysosomal protein deficient in Niemann-Pick type C2 disease. *J. Biol. Chem.* 282, 23525–23531.

Xu, Z., Farver, W., Kodukula, S., and Storch, J. (2008). Regulation of sterol transport between membranes and NPC2. *Biochemistry* 47, 11134–11143.

Zhang, X.C., Liu, M., and Han, L. (2017). Energy coupling mechanisms of AcrB-like RND transporters. *Biophys Rep* 3, 73–84.

Zhang, Y., Bulkley, D.P., Xin, Y., Roberts, K.J., Asarnow, D.E., Sharma, A., Myers, B.R., Cho, W., Cheng, Y., and Beachy, P.A. (2018). Structural Basis for Cholesterol Transport-like Activity of the Hedgehog Receptor Patched. *Cell* 175, 1352-1364.e14.

Zhang, B., Li, J., Yang, X., Wu, L., Zhang, J., Yang, Y., Zhao, Y., Zhang, L., Yang, X., Yang, X., et al. (2019). Crystal Structures of Membrane Transporter MmpL3, an Anti-TB Drug Target. *Cell* 176, 636-648.e13.

Zheng, S.Q., Palovcak, E., Armache, J.-P., Verba, K.A., Cheng, Y., and Agard, D.A. (2017). MotionCor2: anisotropic correction of beam-induced motion for improved cryo-electron microscopy. *Nat. Methods* 14, 331–332.

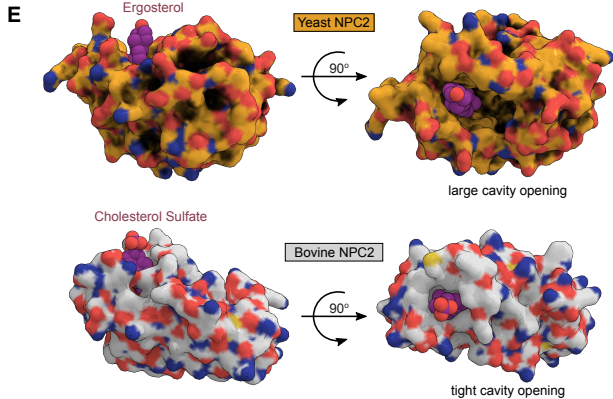
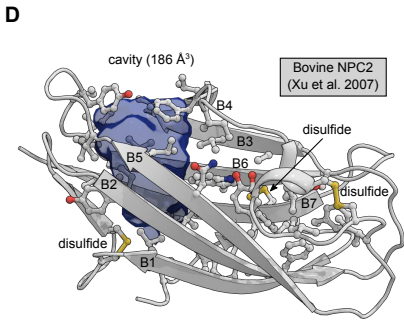
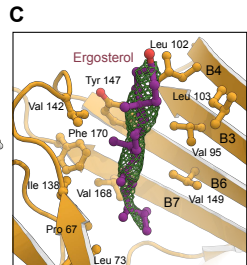
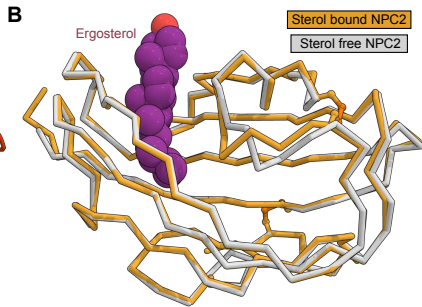
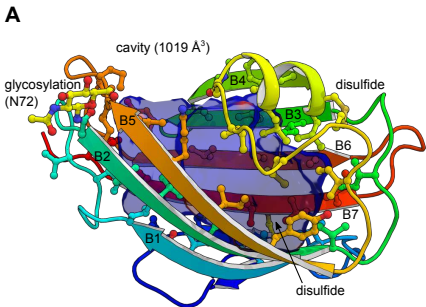


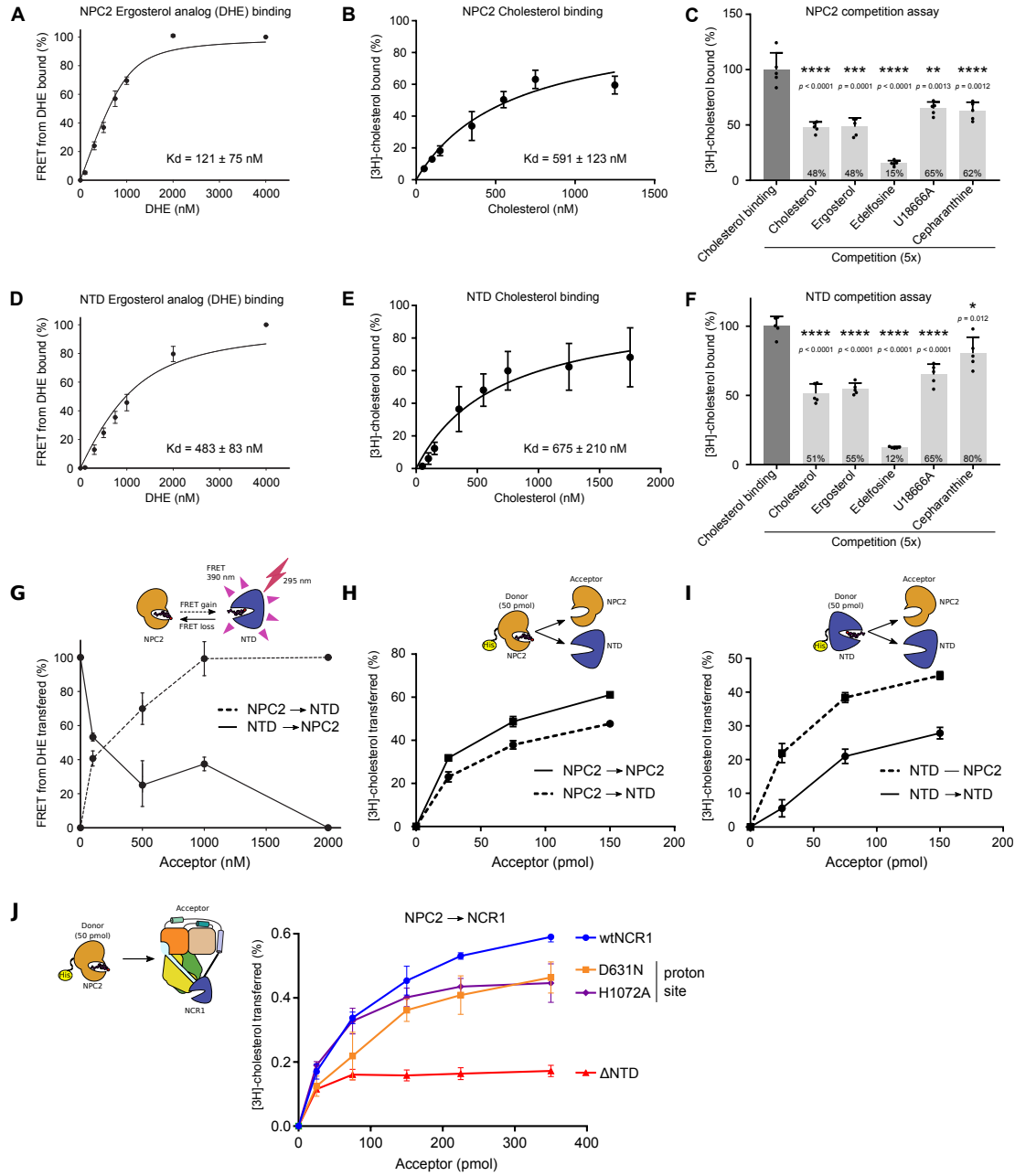
KEY RESOURCES TABLE

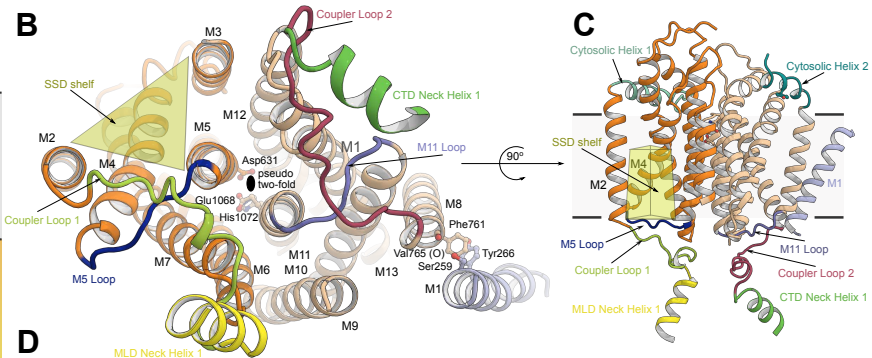
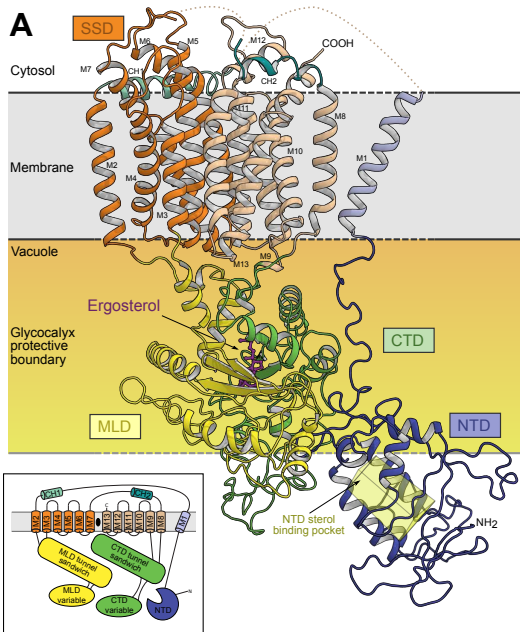
REAGENT or RESOURCE	SOURCE	IDENTIFIER
Chemicals, Peptides, and Recombinant Proteins		
n-Dodecyl- β -D-Maltopyranoside (DDM)	Anatrace	Cat# D310S
Decyl Maltose Neopentyl Glucol (DM-NG)	Anatrace	Cat# NG322
Triton X-100	Sigma	Cat# T8787-100ML
Monoolein	Sigma	Cat# M7765
1,2-dioleoyl-sn-glycero-3-phosphocholine (DOPC)	Avanti Lipids	Cat# 850375
Cholesterol	Sigma	Cat# C8667-5G
[1,2-3H(N)] Cholesterol	Perkin Elmer	Cat# NET139250UC
Ergosterol	Sigma	Cat# 45480-10G-F
Dehydroergosterol	Sigma	Cat# E2634
N-(3-triethylammoniumpropyl)-4-(6-(4-(diethylamino)phenyl)hexatrienyl)pyridinium dibromide (FM4-64)	ThermoFisher	Cat# T3166
(4,4-Difluoro-1,3,5,7,8-Pentamethyl-4-Bora-3a,4a-Diaza-s-Indacene) (BODIPY495/503)	ThermoFisher	Cat# D3922
Concanamycin A	Sigma	Cat# 27689
AnaeroGen	ThermoFisher	Cat# AN0025A
Geneticin™ Selective Antibiotic	ThermoFisher	Cat# 11811031
Endo H	New England Biolabs	Cat# P0702L
PNGase F	Sigma	Cat# P7367
Bovine Thrombin	Sigma	Cat# T7513
Chloroform	Sigma	Cat# 288306-1L
Deposited Data		
NCR1	This paper	PDB: 6R4L
NPC2 sterol-free	This paper	PDB: 6R4M
NPC2 sterol-bound	This paper	PDB: 6R4N
NCR1 EM map	This paper	EMDB: EMD-4771
Experimental Models: Cell Lines		
<i>S. cerevisiae</i> BY4741	Euroscarf culture collection	ACC#: Y00000 http://www.euroscarf.de/plasmid_details.php?accno=Y00000
<i>S. cerevisiae</i> CBY5147 (BY4742 ncr1 Δ ::KanMX4*)	Kindly provided by Dr. Christopher Beh, Simon Fraser University, Canada.	N/A
<i>S. cerevisiae</i> CBY5340 (BY4742 npc2 Δ ::KanMX4*)	Kindly provided by Dr. Christopher Beh, Simon Fraser University, Canada.	N/A
<i>S. cerevisiae</i> DSY-5	Gentaur	Cat# P04003
Recombinant DNA		
p423-GAL1 w. NCR1	This paper	N/A
p423-GAL1 w. NCR1_NTD	This paper	N/A



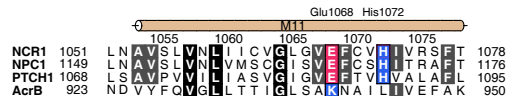
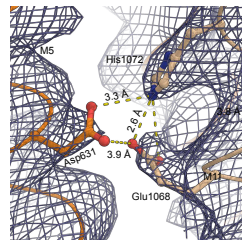
p423-GAL1 w. NPC2	This paper	N/A
Software and Algorithms		
Phenix	Adams et al., 2010	https://www.phenix-online.org/
Phaser	McCoy et al., 2007	http://www.phaser.cimr.cam.ac.uk/index.php/Phaser_Crystallographic_Software
CCP4	Winn et al., 2011	http://www.ccp4.ac.uk/
VMD	Humphrey et al., 1996	https://www.ks.uiuc.edu/Research/vmd/
Namdinator	Kidmose et al., 2019	https://namdinator.au.dk/
Rosetta	DiMaio et al., 2013	https://www.rosettacommons.org/
XDS	Kabsch, 2010	http://xds.mpimf-heidelberg.mpg.de/
Buster	Smart et al., 2012	http://www.globalphasing.com/buster/
MOLE2.0	Sehnal et al., 2013	https://mole.upol.cz/
Coot	Emsley et al., 2010	https://www2.mrc-lmb.cam.ac.uk/personal/pemsley/cool/
Pymol	Schrödinger LLC	https://pymol.org/2/
ImageJ	Schneider et al., 2012	https://imagej.nih.gov/
SigmaPlot	Systat Software Inc.	https://systatsoftware.com/products/sigma-plot/

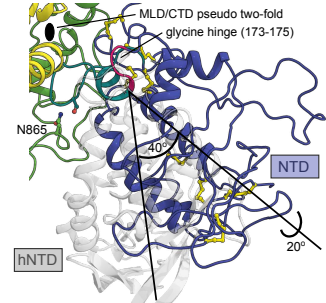
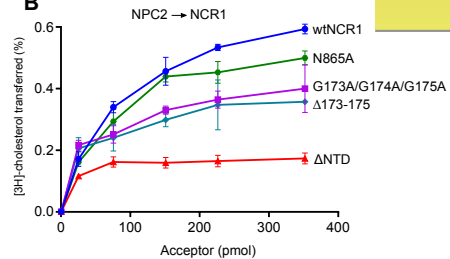
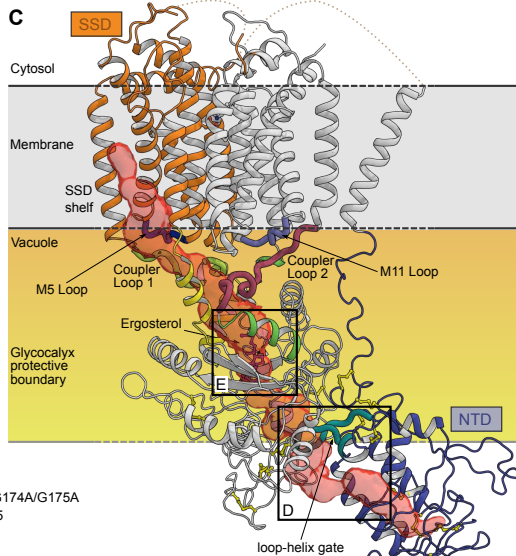
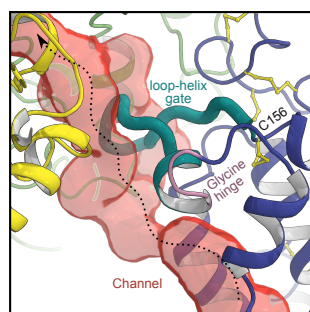
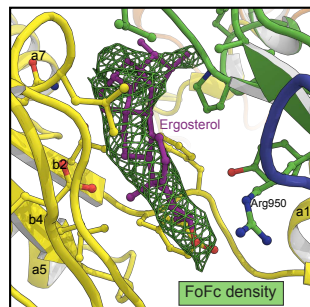


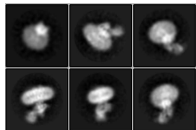
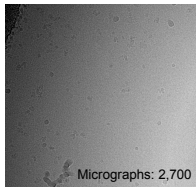
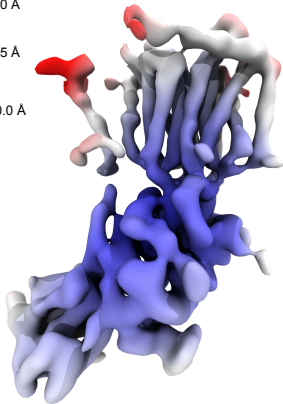
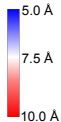
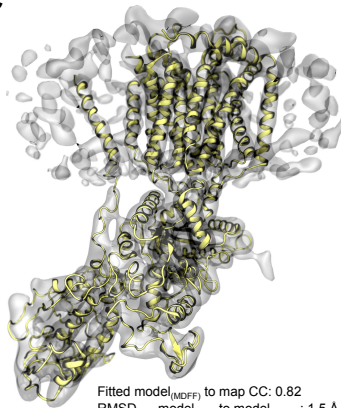


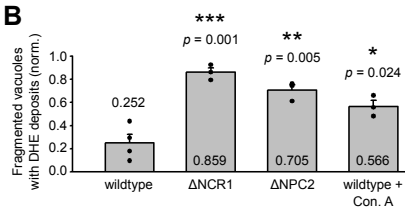
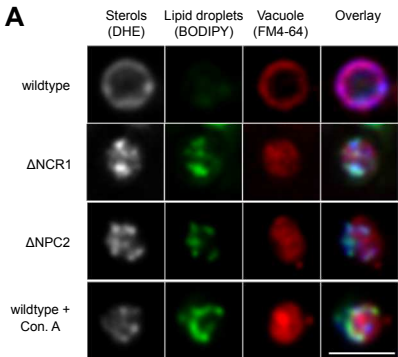


D

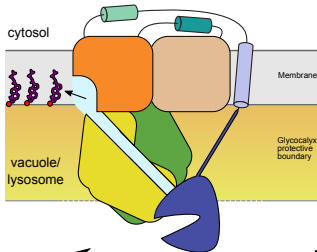


A**B****C****D****E**

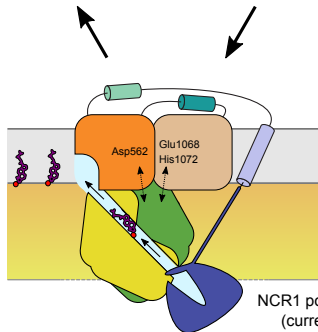
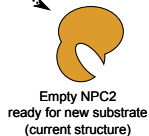
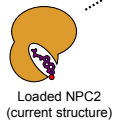
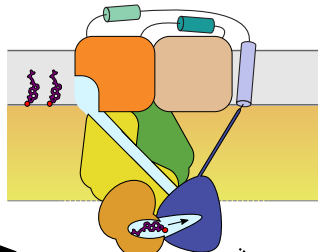
A**B****C**



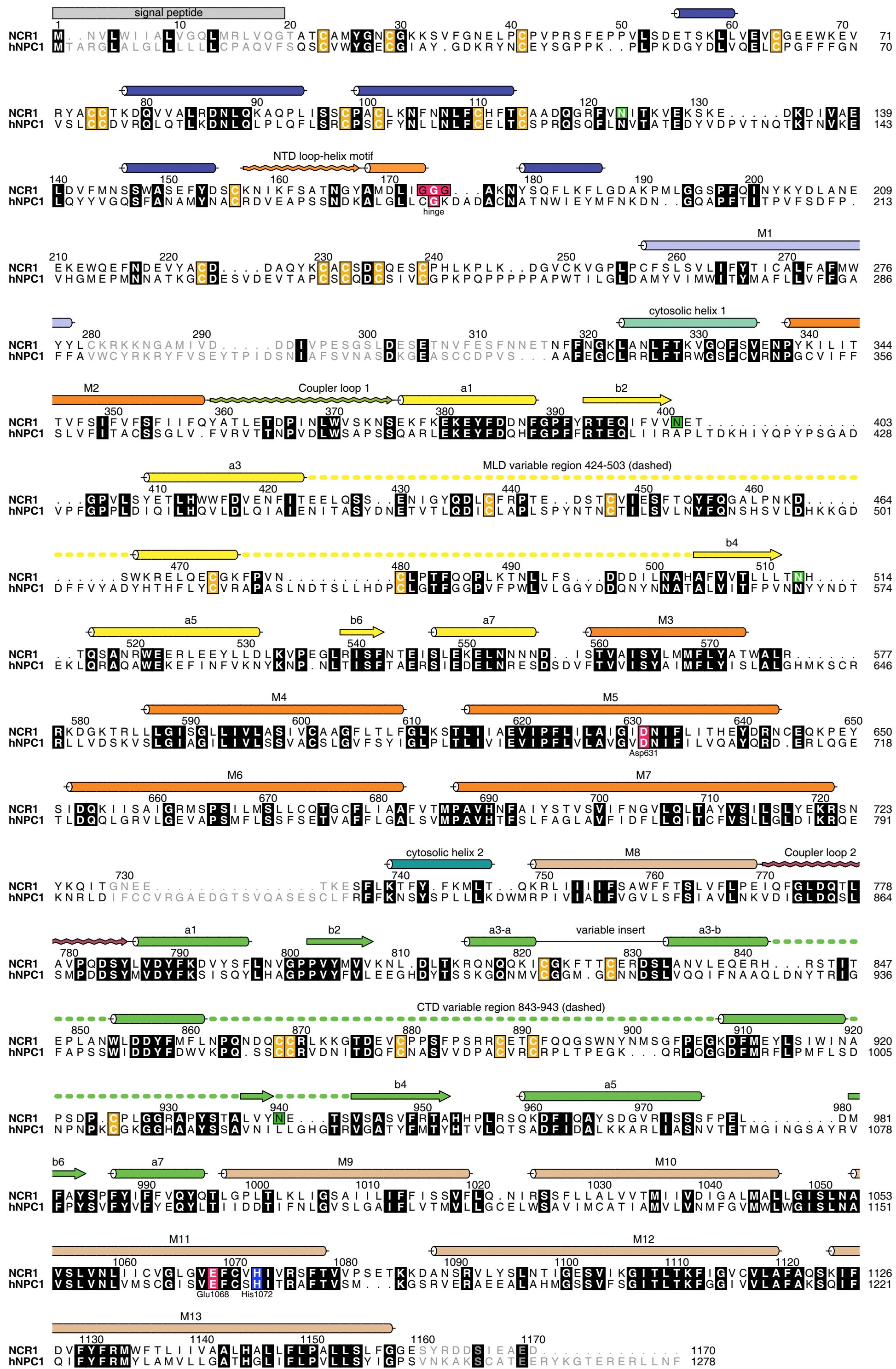
NCR1 pre-loading state
(based on Gong et al 2016)

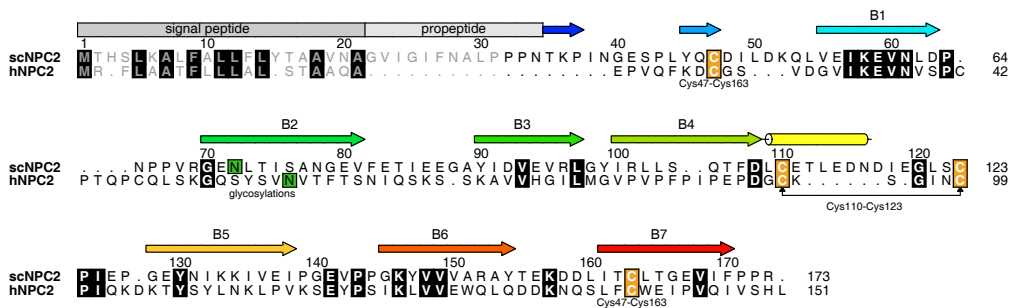
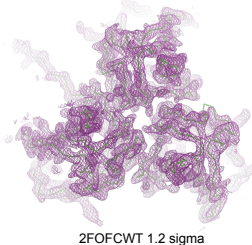
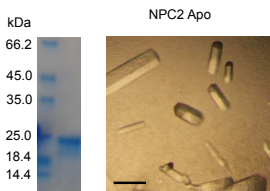
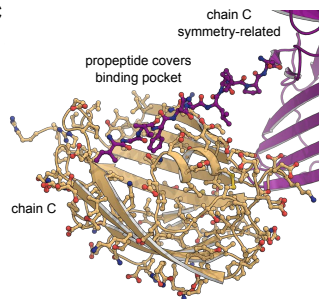


NCR1/NPC2 loading complex
(based on Li et al 2016)

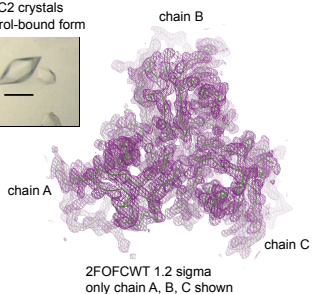
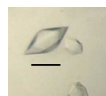


NCR1 post-loading state
(current structure)

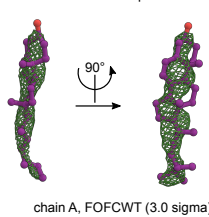


A**B****C****D**

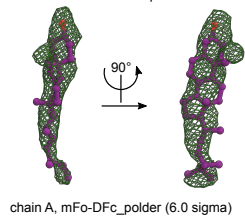
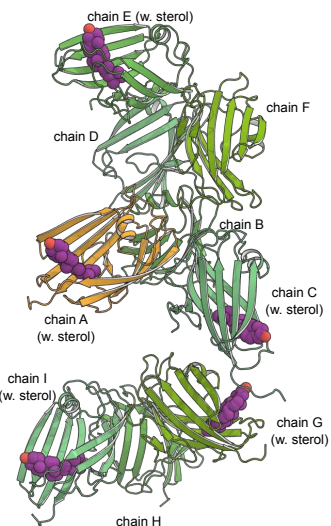
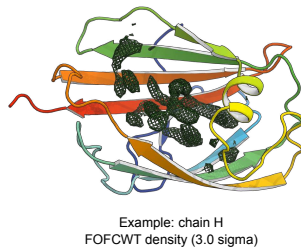
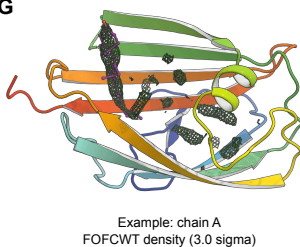
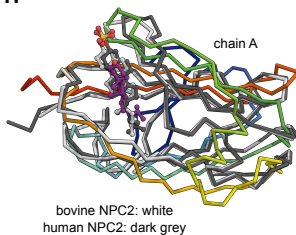
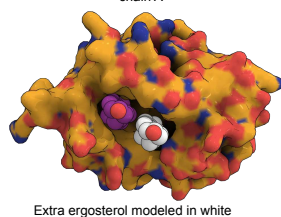
NPC2 crystals
 Sterol-bound form

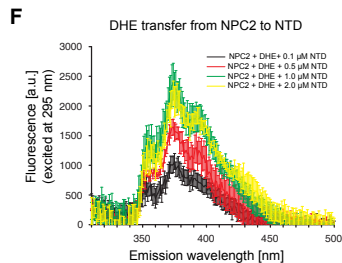
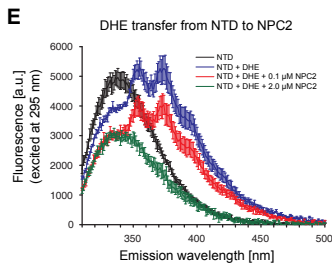
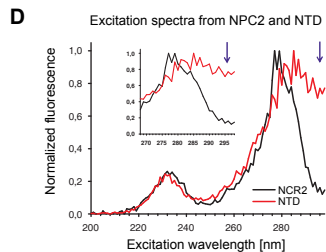
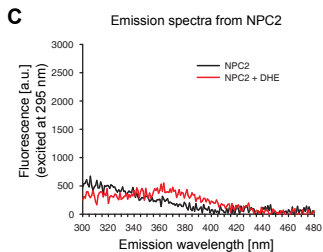
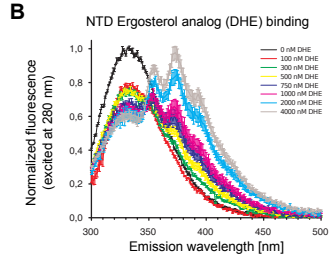
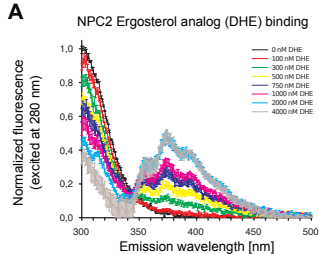
**F**

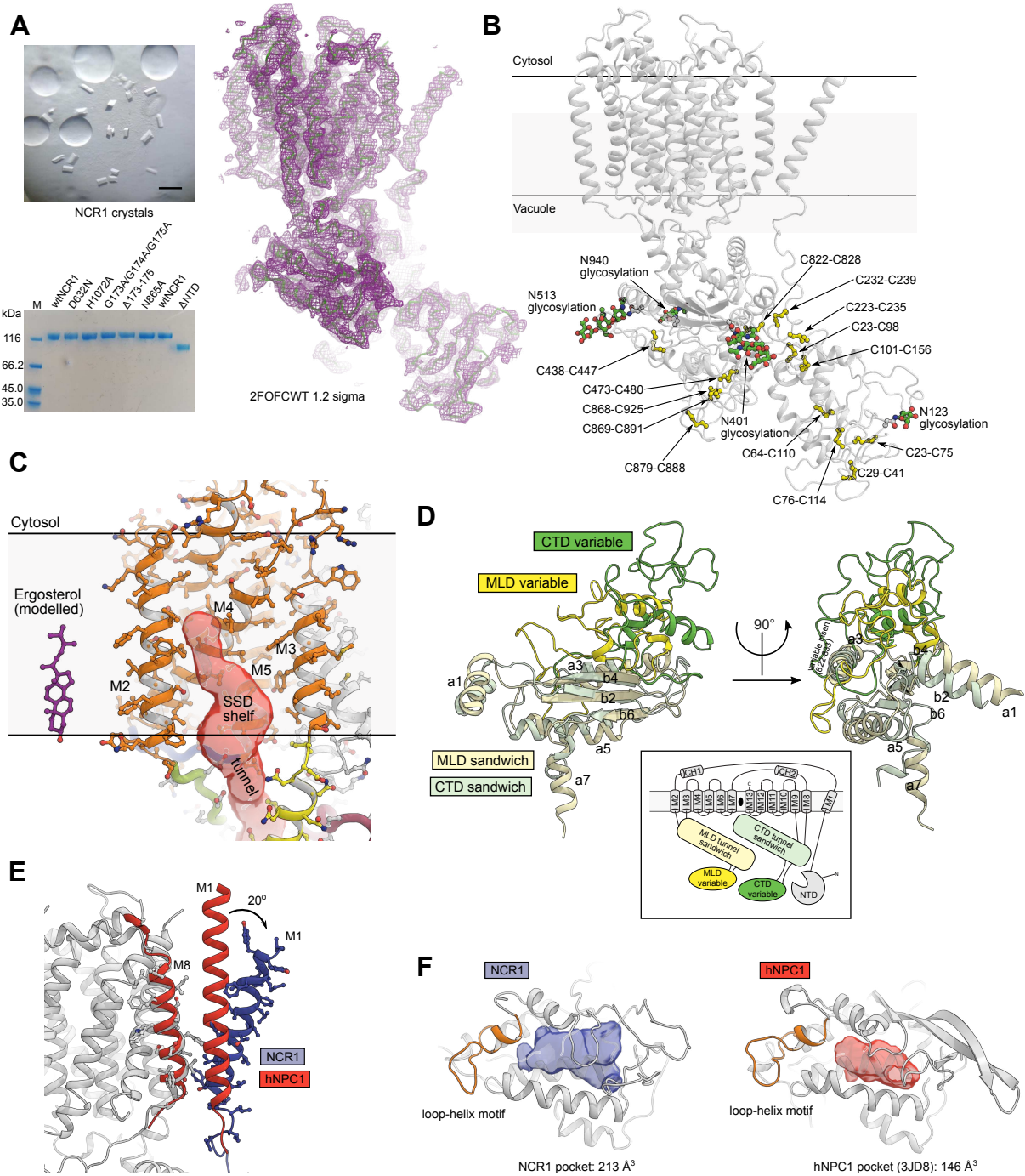
Phenix Omit map

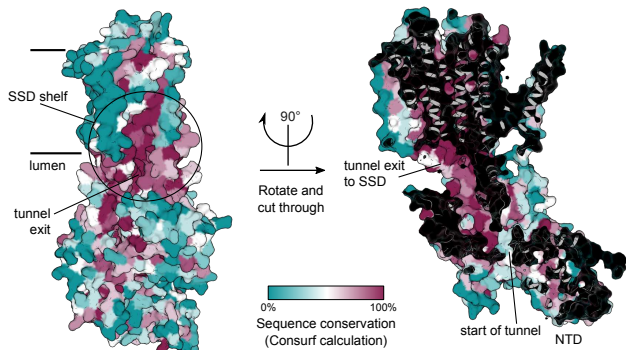
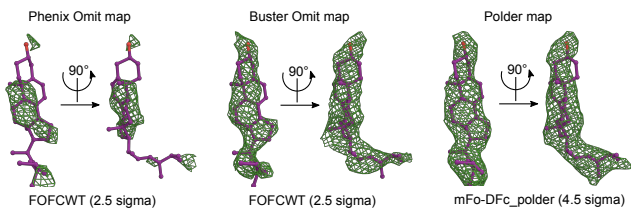
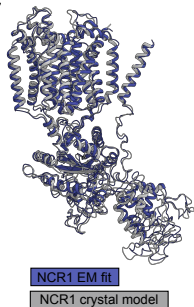
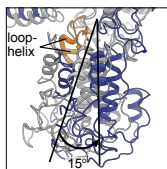
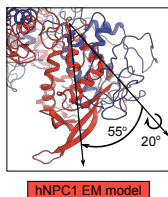
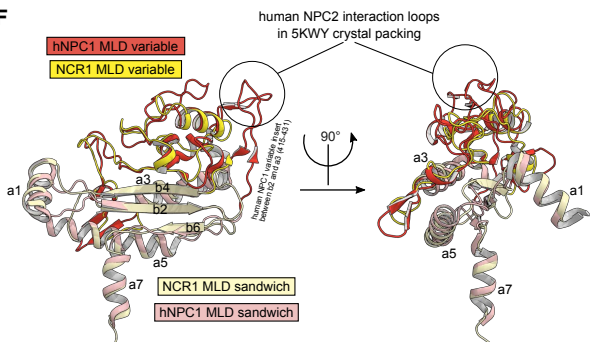


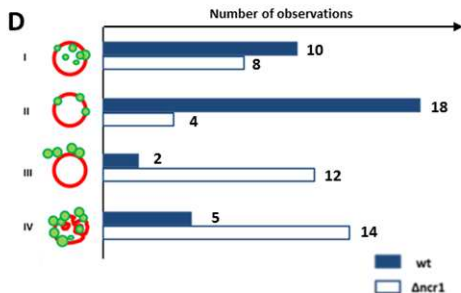
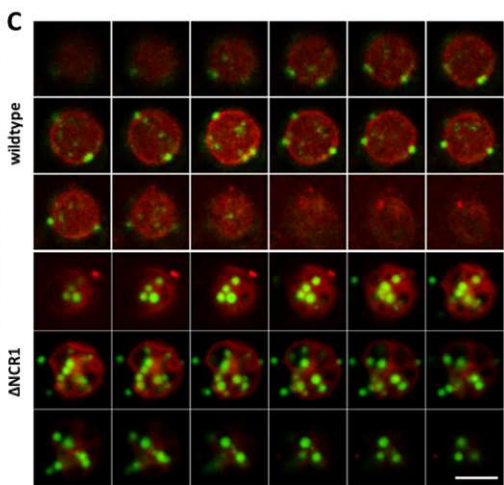
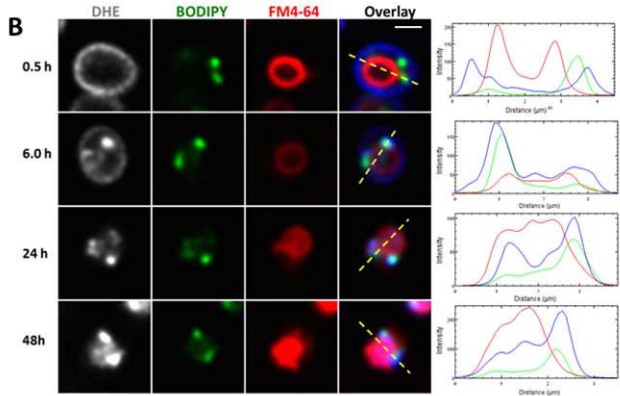
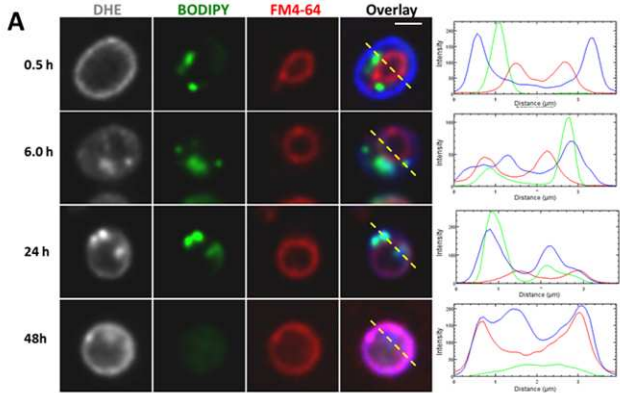
Polder map

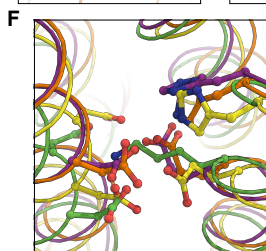
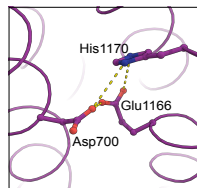
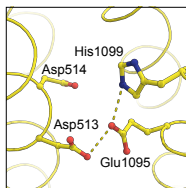
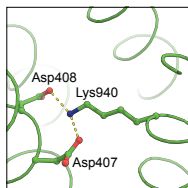
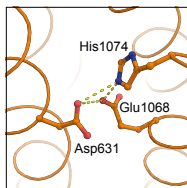
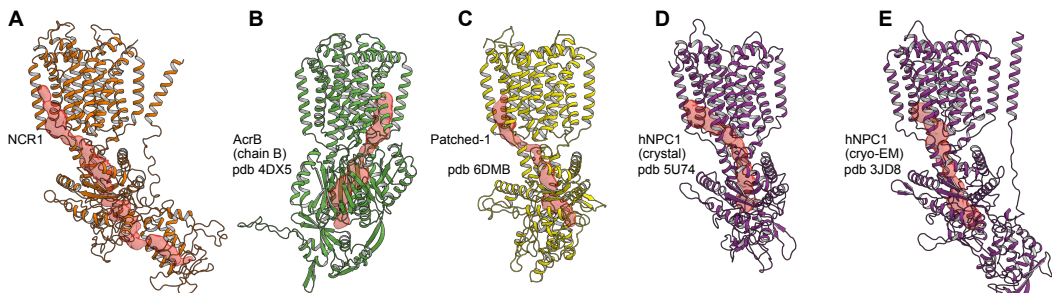
**E****G****H****I**





A**B****C****D****E****F**





Superposition on transmembrane domains (excl. 3JD8)

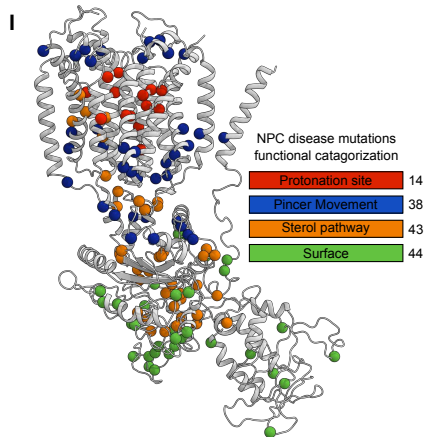
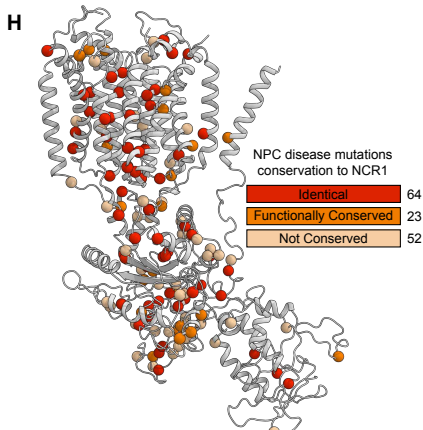
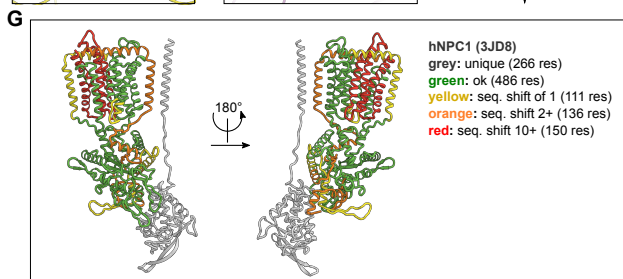


Table S1. Statistics for crystallographic data collection and structure refinement. Related to Figure 1 and Figure 3

Name Type	NCR1 native	NPC2 sterol-free native	NPC2 sterol-bound native	NPC2 Derivative 1 Ta6Br12 derivative	NPC2 Derivative 2 Ta6Br12 derivative
Data Collection					
Space group	C2	P6(1)	P6(1)	P6(1)	P6(2)
Cell dimensions					
a, b, c (Å)	148.7, 90.1, 161.7	205.3, 205.3, 39.1	215.4, 215.4, 129.8	215.5, 215.5, 129.2	194.7, 194.7, 41.3
alpha, beta, gamma (deg)	90.0, 110.3, 90.0	90.0, 90.0, 120.0	90.0, 90.0, 120.0	90.0, 90.0, 120.0	90.0, 90.0, 120.0
Monomers per asym. unit.	1	3	9	9	9
Wavelength (Å)	0.97950	0.97242	0.96864	1.25455	0.97950
Number of reflections measured	43210	88962	880077	540139	178433
Number of unique reflections	23939	23777	75864	100761	16854
Resolution (Å)	49.12-3.5 (3.625-3.5) ^a	44.45-2.8 (2.9-2.8)	48.05-2.9 (3.0-2.9)	49.7-3.3 (3.4-3.3)	56.2-3.9 (4.0-3.9)
Rmeas (%)	7.7 (172.5)	9.16 (168.8)	34.56 (324.2)	22.8 (176.5)	15.4 (378.4)
Mean I/σ(I)	8.55 (0.81)	9.15 (0.73)	8.3 (0.85)	5.49 (0.73)	10.4 (1.3)
CC(1/2)	99.9 (42.8)	99.8 (36.7)	99.3 (27.9)	99.5 (35.6)	99.3 (81.5)
Completeness (%)	93.5 (96.4)	99.54 (99.4)	99.91 (99.93)	99.9 (99.7)	99.60 (99.87)
Redundancy	1.8 (1.8)	3.7 (3.2)	11.6 (11.6)	5.4 (5.4)	11.2 (10.7)
Wilson B-factor (Å)	134	90	66		
Refinement					
Resolution (Å)	49.12-3.5 (3.6-3.5)	44.45-2.8 (2.9-2.8)	48.05-2.9 (3.0-2.9)		
No. reflections (work/free)	22663/1209	22585/1197	73868/1990		
Rwork (%)	26.56 (37.31)	23.63 (37.28)	22.58 (34.31)		
Rfree (%)	30.12 (41.81)	26.18 (40.78)	25.67 (36.50)		
No. of Atoms					
Protein	8759	3389	10121		
Ergosterol	29	n/a	145		
Carbohydrates / Ions	106	42	220		
Average B Factors (Å)					
Overall	158	108	70		
Protein	157	107	68		
Ergosterol	157	n/a	93		
Carbohydrates / Ions	231	172	131		
RMSD					
Bond lengths (Å)	0.010	0.007	0.011		
Bond angles (deg)	1.12	1.25	1.42		
Ramachandran Plot Statistics					
Favored regions	92.1	96.0	97.0		
Allowed regions	7.7	3.5	2.9		
Disallowed regions	0.2	0.5	0.1		
Deposited model (PDB id)	6R4L	6R4M	6R4N		

^aHighest resolution shell is shown in parenthesis.

Table S2 - Niedmann-Pick Disease type C missense mutations identified in literature. Related to Figure 4 and Figure 6

Human NPC1 residue	Disease mutation	Location	Functional categorization	Corresponding residue in NCR1*	References [PMID]
63	C → R	NTD	Surface	C64	Meiner V et al. (2001) [11545687]
74	C → Y	NTD	Surface	C75	Park WD et al. (2003) [12955717]
92	Q → R	NTD	Surface	P93	Sun X et al. (2001) [11349231]; Ribeiro I et al. (2001) [11479732]
113	C → R	NTD	Surface	C114	Blom TS et al. (2003) [12554680]
137	T → M	NTD	Surface	D133	Sun X et al. (2001) [11349231]; Fernandez-Valero EM et al. (2005) [16098014]; Akizu N et al. (2013) [23453666]
166	P → S	NTD	Sterol Pathway	S162	Park WD et al. (2003) [12955717]; Millat G et al. (2005) [16126423]
177	C → G	NTD	Sterol Pathway	G174	Yamamoto T et al. (2000) [11182931]
177	C → Y	NTD	Sterol Pathway	G174	Ribeiro I et al. (2001) [11479732]; Fernandez-Valero EM et al. (2005) [16098014]; Millat G et al. (2005) [16126423]
215	H → R	NTD	Surface	K211	Wassif CA et al. (2016) [25764212]
222	N → S	NTD	Surface	D218	Park WD et al. (2003) [12955717]
231	V → G	NTD	Surface	-	Kaminski WE et al. (2002) [12408188]
242	D → H	NTD	Surface	D234	Millat G et al. (2001) [11333381]
242	D → N	NTD	Surface	D234	Sun X et al. (2001) [11349231]
247	C → Y	NTD	Surface	C239	Park WD et al. (2003) [12955717]
248	G → V	NTD	Surface	P240	Sun X et al. (2001) [11349231]
272	M → R	M1 helix	Surface	V262	Millat G et al. (2001) [11333381]
372	R → W	MLD	Pincer movement	T361	Fernandez-Valero EM et al. (2005) [16098014]
378	V → A	MLD	Sterol Pathway	I367	Millat G et al. (2001) [11333381]
380	L → F	MLD	Sterol Pathway	L369	Park WD et al. (2003) [12955717]
388	A → P	MLD	Pincer movement	K377	Park WD et al. (2003) [12955717]
389	R → C	MLD	Pincer movement	F378	Park WD et al. (2003) [12955717]
401	P → T	MLD	Sterol Pathway	P390	Sun X et al. (2001) [11349231]
404	R → P	MLD	Sterol Pathway	R393	Millat G et al. (2005) [16126423]
404	R → Q	MLD	Sterol Pathway	R393	Sun X et al. (2001) [11349231]; Millat G et al. (2001) [11333381]; Meiner V et al. (2001) [115456879]
404	R → W	MLD	Sterol Pathway	R393	Park WD et al. (2003) [12955717]
433	P → L	MLD	Surface	P405	Park WD et al. (2003) [12955717]
434	P → L	MLD	Surface	V406	Fernandez-Valero EM et al. (2005) [16098014]
451	E → K	MLD	Surface	T423	Tarugi P et al. (2002) [12401890]
473	S → P	MLD	Surface	E443	Yamamoto T et al. (2000) [11182931]
474	P → L	MLD	Surface	-	Fernandez-Valero EM et al. (2005) [16098014]; Tarugi P et al. (2002) [12401890]
479	C → Y	MLD	Surface	G447	Fernandez-Valero EM et al. (2005) [16098014]
509	Y → S	MLD	Surface	W466	Park WD et al. (2003) [12955717]
510	H → P	MLD	Surface	K467	Yamamoto T et al. (2000) [11182931]
512	H → R	MLD	Surface	E469	Bauer P et al. (2002) [11754101]
518	R → Q	MLD	Sterol Pathway	K475	Yamamoto T et al. (2000) [11182931]; Millat G et al. (2001) [11333381]
518	R → W	MLD	Sterol Pathway	K475	Ribeiro I et al. (2001) [11479732]; Gong X et al. (2016) [27238017]
521	A → S	MLD	Sterol Pathway	V478	Park WD et al. (2003) [12955717]
537	F → L	MLD	Surface	F483	Millat G et al. (2005) [16126423]
543	P → L	MLD	Sterol Pathway	T490	Park WD et al. (2003) [12955717]; Millat G et al. (2005) [16126423]
576	K → R	MLD	Surface	-	Fernandez-Valero EM et al. (2005) [16098014]
605	A → V	MLD	Sterol Pathway	T544	Millat G et al. (2001) [11333381]
612	E → D	MLD	Pincer movement	E551	Sun X et al. (2001) [11349231]
615	R → C	MLD	Pincer movement	N554	Millat G et al. (2005) [16126423]
615	R → L	MLD	Pincer movement	N554	Park WD et al. (2003) [12955717]; Millat G et al. (2005) [16126423]
628	Y → C	SSD	Pincer movement	Y565	Garver WS et al. (2010) [19744920]
631	M → R	SSD	Protonation site	M567	Millat G et al. (2005) [16126423]; Millat G et al. (2001) [11333381]
640	G → R	SSD	Pincer movement	R577	Park WD et al. (2003) [12955717]
652	S → W	SSD	Pincer movement	T583	Sun X et al. (2001) [11349231]
660	G → S	SSD	Sterol Pathway	G591	Park WD et al. (2003) [12955717]
664	V → M	SSD	Sterol Pathway	V595	Park WD et al. (2003) [12955717]; Fernandez-Valero EM et al. (2005) [16098014]
666	S → N	SSD	Sterol Pathway	A597	Dvorakova L et al. (2006) [16802107]
670	C → W	SSD	Pincer movement	C601	Bauer P et al. (2002) [11754101]
673	G → V	SSD	Pincer movement	G604	Park WD et al. (2003) [12955717]
684	L → F	SSD	Sterol Pathway	L615	Park WD et al. (2003) [12955717]
691	P → L	SSD	Sterol Pathway	P622	Park WD et al. (2003) [12955717]
695	L → V	SSD	Sterol Pathway	L626	Park WD et al. (2003) [12955717]
700	D → N	SSD	Protonation site	D631	Park WD et al. (2003) [12955717]
703	F → S	SSD	Protonation site	F634	Yamamoto T et al. (2000) [11182931]
724	L → P	SSD	Pincer movement	I656	Millat G et al. (2001) [11333381]
727	V → F	SSD	Pincer movement	A659	Fernandez-Valero EM et al. (2005) [16098014]
734	S → I	SSD	Protonation site	S665	Park WD et al. (2003) [12955717]
742	E → K	SSD	Protonation site	Q674	Park WD et al. (2003) [12955717]
745	A → E	SSD	Protonation site	C677	Park WD et al. (2003) [12955717]
754	M → K	SSD	Pincer movement	M685	Fernandez-Valero EM et al. (2005) [16098014]
763	F → L	SSD	Pincer movement	Y695	Millat G et al. (2005) [16126423]
767	A → V	SSD	Pincer movement	S699	Park WD et al. (2003) [12955717]
775	Q → P	SSD	Protonation site	Q707	Fernandez-Valero EM et al. (2005) [16098014]; Millat G et al. (2001) [11333381]
789	R → C	SSD	Pincer movement	R721	Sun X et al. (2001) [11349231]
789	R → G	SSD	Pincer movement	R721	Park WD et al. (2003) [12955717]
825	Y → C	SSD	Pincer movement	Y742	Sun X et al. (2001) [11349231]; Millat G et al. (2005) [16126423]; Millat G et al. (2001) [11333381]; Bauer P et al. (2002) [11754101]
849	S → I	SSD	Pincer movement	S763	Bauer P et al. (2002) [11754101]
862	Q → L	CTD	Sterol Pathway	Q776	Millat G et al. (2005) [16126423]
865	S → L	CTD	Sterol Pathway	A779	Fernandez-Valero EM et al. (2005) [16098014]; Millat G et al. (2005) [16126423]
871	Y → C	CTD	Pincer movement	Y785	Millat G et al. (2005) [16126423]
874	D → V	CTD	Pincer movement	D788	Sun X et al. (2001) [11349231]; Kaminski WE et al. (2002) [12408188]; Millat G et al. (2001) [11333381]; Bauer P et al. (2002) [11754101]
887	P → L	CTD	Pincer movement	P801	Garver WS et al. (2010) [19744920]
888	P → S	CTD	Sterol Pathway	P802	Sun X et al. (2001) [11349231]
889	V → M	CTD	Sterol Pathway	V803	Yamamoto T et al. (2000) [11182931]
890	Y → C	CTD	Sterol Pathway	Y804	Tarugi P et al. (2002) [12401890]
899	Y → D	CTD	Sterol Pathway	L812	Tarugi P et al. (2002) [124018909]
910	G → S	CTD	Sterol Pathway	G823	Tarugi P et al. (2002) [12401890]
917	D → Y	CTD	Surface	D831	Millat G et al. (2005) [16126423]

923	I → V	CTD	Surface	L837	Garver WS et al. (2010) [19744920]
926	A → T	CTD	Sterol Pathway	E840	Fernandez-Valero EM et al. (2005) [16098014]
927	A → V	CTD	Sterol Pathway	R841	Meiner V et al. (2001) [11545687]
928	Q → P	CTD	Sterol Pathway	H842	Carstea ED et al. (1997) [9211849]
929	L → P	CTD	Surface	-	Sun X et al. (2001) [11349231]
934	R → Q	CTD	Surface	T845	Millat G et al. (2005) [16126423]; Millat G et al. (2001) [11333381]; Greer WL et al. (1999) [10521290]
940	S → L	CTD	Sterol Pathway	A851	Sun X et al. (2001) [11349231]; Millat G et al. (2005) [16126423]; Greer WL et al. (1999) [10521290]
942	W → C	CTD	Sterol Pathway	W853	Ribeiro I et al. (2001) [11479732]; Fernandez-Valero EM et al. (2005) [16098014]
943	I → M	CTD	Sterol Pathway	L854	Millat G et al. (2001) [11333381]
944	D → N	CTD	Sterol Pathway	D855	Sun X et al. (2001) [11349231]; Fernandez-Valero EM et al. (2005) [16098014]; Millat G et al. (2001) [11333381]
945	D → N	CTD	Sterol Pathway	D856	Park WD et al. (2003) [12955717]
948	D → H	CTD	Sterol Pathway	M859	Fernandez-Valero EM et al. (2005) [16098014]
948	D → N	CTD	Sterol Pathway	M859	Sun X et al. (2001) [11349231]; Kaminski WE et al. (2002) [12408188]; Greer WL et al. (1999) [10521290]
948	D → Y	CTD	Sterol Pathway	M859	Bauer P et al. (2002) [11754101]
950	V → M	CTD	Surface	L861	Millat G et al. (2005) [16126423]; Millat G et al. (2001) [11333381]
954	S → L	CTD	Surface	D866	Yamamoto T et al. (2000) [11182931]; Bauer P et al. (2002) [11754101]; Greer WL et al. (1999) [10521290]
956	C → Y	CTD	Surface	C868	Yamamoto T et al. (2000) [11182931]
958	R → L	CTD	Surface	Y870	Bauer P et al. (2002) [11754101]
958	R → Q	CTD	Surface	R870	Sun X et al. (2001) [11349231]
959	V → E	CTD	Surface	L871	Fernandez-Valero EM et al. (2005) [16098014]
961	N → S	CTD	Surface	K873	Dvorakova L et al. (2006) [16802107]
968	N → S	CTD	Surface	P880	Millat G et al. (2005) [16126423]; Yang CC et al. (2005) [15774455]
976	C → R	CTD	Surface	C888	Sun X et al. (2001) [11349231]
978	R → C	CTD	Surface	T890	Sun X et al. (2001) [11349231]; Ribeiro I et al. (2001) [11479732]
986	G → S	CTD	Surface	N898	Millat G et al. (2001) [11333381]
992	G → A	CTD	Surface	G907	Millat G et al. (2005) [16126423]
992	G → R	CTD	Surface	G907	Millat G et al. (2001) [11333381]; Millat G et al. (2005) [16126423]
992	G → W	CTD	Surface	G907	Meiner V et al. (2001) [11545687]; Millat G et al. (2005) [16126423]; Tarugi P et al. (2002) [12401890]; Greer WL (1999) [10521290]; Greer WL (1998) [9634529]
996	M → R	CTD	Surface	M911	Yamamoto T et al. (2000) [11182931]
1004	S → L	CTD	Surface	N919	Sun X et al. (2001) [11349231]
1007	P → A	CTD	Sterol Pathway	S922	Ribeiro I et al. (2001) [11479732]; Fernandez-Valero EM et al. (2005) [16098014]; Millat G et al. (2005) [16126423]; Millat G et al. (2001) [11333381]; Tarugi P et al. (2002) [12401890]; Bauer P et al. (2002) [11754101]; Greer WL et al. (1999) [10521290]
1012	G → D	CTD	Sterol Pathway	P926	Meiner V et al. (2001) [11545687]
1015	G → V	CTD	Sterol Pathway	G929	Yang CC et al. (2005) [15774455]
1016	H → R	CTD	Sterol Pathway	R930	Park WD et al. (2003) [12955717]
1023	V → G	CTD	Sterol Pathway	L937	Sun X et al. (2001) [11349231]
1034	G → R	CTD	Sterol Pathway	S945	Yang CC et al. (2005) [15774455]
1035	A → V	CTD	Sterol Pathway	A946	Ribeiro I et al. (2001) [11479732]; Fernandez-Valero EM et al. (2005) [16098014]
1036	T → K	CTD	Sterol Pathway	S947	Fernandez-Valero EM et al. (2005) [16098014]
1036	T → M	CTD	Sterol Pathway	S947	Fernandez-Valero EM et al. (2005) [16098014]; Millat G et al. (2005) [16126423]
1054	A → T	CTD	Pincer movement	A965	Millat G et al. (2001) [11333381]
1059	R → Q	CTD	Pincer movement	V970	Park WD et al. (2003) [12955717]
1061	I → T	CTD	Surface	I972	Sun X et al. (2001) [11349231]; Ribeiro I et al. (2001) [11479732]; Fernandez-Valero EM et al. (2005) [16098014]; Millat G et al. (2005) [16126423]; Yamamoto T et al. (2000) [11182931]; Millat G et al. (2001) [11333381]; Tarugi P et al. (2002) [12401890]; Bauer P et al. (2002) [11754101]; Greer WL et al. (1999) [10521290]; Millat G et al. (2005) [16126423]
1062	A → V	CTD	Surface	S973	Millat G et al. (2005) [16126423]
1066	T → N	CTD	Surface	P977	Fernandez-Valero EM et al. (2005) [16098014]
1087	F → L	CTD	Sterol Pathway	F990	Park WD et al. (2003) [12955717]
1088	Y → C	CTD	Sterol Pathway	F991	Yamamoto T et al. (2000) [11182931]
1089	E → K	CTD	Sterol Pathway	V992	Sun X et al. (2001) [11349231]
1094	I → T	SSD-like	Pincer movement	L997	Kaminski WE et al. (2002) [12408188]
1097	D → N	SSD-like	Pincer movement	L1000	Millat G et al. (2005) [16126423]
1137	N → I	SSD-like	Pincer movement	D1039	Park WD et al. (2003) [12955717]
1140	G → V	SSD-like	Pincer movement	A1042	Park WD et al. (2003) [12955717]
1142	M → T	SSD-like	Pincer movement	M1044	Sun X et al. (2001) [11349231]; Millat G et al. (2001) [11333381]
1150	N → K	SSD-like	Pincer movement	N1052	Sun X et al. (2001) [11349231]
1151	A → T	SSD-like	Pincer movement	A1053	Garver WS et al. (2010) [19744920]
1156	N → I	SSD-like	Protonation site	N1058	Fernandez-Valero EM et al. (2005) [16098014]
1156	N → S	SSD-like	Protonation site	N1058	Sun X et al. (2001) [11349231]; Meiner V et al. (2001) [11545687]; Fernandez-Valero EM et al. (2005) [16098014]; Tarugi P et al. (2002) [12401890]
1165	V → M	SSD-like	Protonation site	V1067	Sun X et al. (2001) [11349231]
1167	F → L	SSD-like	Protonation site	F1069	Imrie J et al. (2007) [17160617]
1168	C → Y	SSD-like	Protonation site	C1070	Millat G et al. (2001) [11333381]
1174	A → V	SSD-like	Pincer movement	S1076	Millat G et al. (2005) [16126423]
1186	R → H	SSD-like	Pincer movement	R1091	Sun X et al. (2001) [11349231]; Millat G et al. (2005) [16126423]; Millat G et al. (2001) [11333381]
1189	E → G	SSD-like	Pincer movement	Y1094	Sun X et al. (2001) [11349231]
1205	T → K	SSD-like	Protonation site	T1110	Park WD et al. (2003) [12955717]
1205	T → R	SSD-like	Protonation site	T1110	Yamamoto T et al. (2000) [11182931]
1212	V → L	SSD-like	Pincer movement	V1117	Yang CC et al. (2005) [15774455]
1213	L → V	SSD-like	Pincer movement	L1118	Greer WL et al. (1999) [10521290]
1213	L → F	SSD-like	Pincer movement	L1118	Yamamoto T et al. (2000) [11182931]
1216	A → V	SSD-like	Pincer movement	A1121	Millat G et al. (2005) [16126423]
1224	F → L	SSD-like	Pincer movement	F1126	Fernandez-Valero EM et al. (2005) [16098014]
1236	G → E	SSD-like	Protonation site	A1141	Yamamoto T et al. (2000) [11182931]
1240	G → R	SSD-like	Protonation site	A1145	Millat G et al. (2005) [16126423]
1249	S → G	SSD-like	Pincer movement	S1154	Park WD et al. (2003) [12955717]

*Colorcoding according to conservation. Red, residue identical between hNPC1 and NCR1; orange, residue functionally conserved between hNPC1 and NCR1; wheat, residue not conserved. Functional conservation clustering is based on chemical properties with the following groups: Aromatic (F, W, Y), polar (S, T, N, Q, C), pos. charged (R, H, K), neg. charged (D, E), hydrophobic (A, V, I, L, M, G), special (P).